



ALMA Lensing Cluster Survey

Full Spectral Energy Distribution Analysis of $z = 0.5-6$ Lensed Galaxies Detected with millimeter Observations

Uematsu, Ryosuke; Ueda, Yoshihiro; Kohno, Kotaro; Toba, Yoshiki; Yamada, Satoshi; Smail, Ian; Umehata, Hideki; Fujimoto, Seiji; Hatsukade, Bunyo; Ao, Yiping

Total number of authors:
20

Published in:
Astrophysical Journal

Link to article, DOI:
[10.3847/1538-4357/ad26f7](https://doi.org/10.3847/1538-4357/ad26f7)

Publication date:
2024

Document Version
Publisher's PDF, also known as Version of record

[Link back to DTU Orbit](#)

Citation (APA):

Uematsu, R., Ueda, Y., Kohno, K., Toba, Y., Yamada, S., Smail, I., Umehata, H., Fujimoto, S., Hatsukade, B., Ao, Y., Bauer, F. E., Brammer, G., Dessauges-Zavadsky, M., Espada, D., Jolly, J. B., Koekemoer, A. M., Kokorev, V., Magdis, G. E., Oguri, M., & Sun, F. (2024). ALMA Lensing Cluster Survey: Full Spectral Energy Distribution Analysis of $z = 0.5-6$ Lensed Galaxies Detected with millimeter Observations. *Astrophysical Journal*, 965(2), Article 108. <https://doi.org/10.3847/1538-4357/ad26f7>

General rights

Copyright and moral rights for the publications made accessible in the public portal are retained by the authors and/or other copyright owners and it is a condition of accessing publications that users recognise and abide by the legal requirements associated with these rights.

- Users may download and print one copy of any publication from the public portal for the purpose of private study or research.
- You may not further distribute the material or use it for any profit-making activity or commercial gain
- You may freely distribute the URL identifying the publication in the public portal

If you believe that this document breaches copyright please contact us providing details, and we will remove access to the work immediately and investigate your claim.



ALMA Lensing Cluster Survey: Full Spectral Energy Distribution Analysis of $z \sim 0.5-6$ Lensed Galaxies Detected with millimeter Observations

Ryosuke Uematsu¹, Yoshihiro Ueda¹, Kotaro Kohno^{2,3}, Yoshiki Toba^{4,5,6}, Satoshi Yamada⁷, Ian Smail⁸, Hideki Umehata^{9,10}, Seiji Fujimoto^{11,12,13}, Bunyo Hatsukade², Yiping Ao¹⁴, Franz Erik Bauer^{15,16,17,18}, Gabriel Brammer^{12,13}, Miroslava Dessauges-Zavadsky¹⁹, Daniel Espada^{20,21}, Jean-Baptiste Jolly²², Anton M. Koekemoer²³, Vasily Kokorev^{12,13,24}, Georgios E. Magdis^{12,13,17,25}, Masamune Oguri^{26,27}, and Fengwu Sun²⁸

¹ Department of Astronomy, Kyoto University, Kyoto 606-8502, Japan; uematsu@kustro.kyoto-u.ac.jp

² Institute of Astronomy, Graduate School of Science, The University of Tokyo, 2-21-1 Osawa, Mitaka, Tokyo 181-0015, Japan

³ Research Center for the Early Universe, School of Science, The University of Tokyo, 7-3-1 Hongo, Bunkyo-ku, Tokyo 113-0033, Japan

⁴ National Astronomical Observatory of Japan, 2-21-1 Osawa, Mitaka, Tokyo 181-8588, Japan

⁵ Academia Sinica Institute of Astronomy and Astrophysics, 11F of Astronomy-Mathematics Building, AS/NTU, No.1, Section 4, Roosevelt Road, Taipei 10617, Taiwan

⁶ Research Center for Space and Cosmic Evolution, Ehime University, 2-5 Bunkyo-cho, Matsuyama, Ehime 790-8577, Japan

⁷ Institute of Physical and Chemical Research (RIKEN), 2-1 Hirosawa, Wako, Saitama 351-0198, Japan

⁸ Centre for Extragalactic Astronomy, Department of Physics, Durham University, South Road, Durham, DH1 3LE, UK

⁹ Institute for Advanced Research, Nagoya University, Furocho, Chikusa, Nagoya 464-8602, Japan

¹⁰ Department of Physics, Nagoya University, Furo-cho, Chikusa-ku, Nagoya 464-8601, Japan

¹¹ Department of Astronomy, The University of Texas at Austin, Austin, TX, USA

¹² Cosmic Dawn Center (DAWN), Denmark

¹³ Niels Bohr Institute, University of Copenhagen, Copenhagen N, Denmark

¹⁴ Purple Mountain Observatory and Key Laboratory for Radio Astronomy, Chinese Academy of Sciences, Nanjing, People's Republic of China

¹⁵ Instituto de Astrofísica, Facultad de Física, Pontificia Universidad Católica de Chile, Campus San Joaquín, Av. Vicuña Mackenna 4860, Macul Santiago, 7820436, Chile

¹⁶ Centro de Astroingeniería, Facultad de Física, Pontificia Universidad Católica de Chile, Campus San Joaquín, Av. Vicuña Mackenna 4860, Macul Santiago, 7820436, Chile

¹⁷ Millennium Institute of Astrophysics, Nuncio Monseñor Sótero Sanz 100, Of 104, Providencia, Santiago, Chile

¹⁸ Space Science Institute, 4750 Walnut Street, Suite 205, Boulder, CO 80301, USA

¹⁹ Department of Astronomy, University of Geneva, 51 chemin Pegasi, 1290 Versoix, Switzerland

²⁰ Departamento de Física Teórica y del Cosmos, Campus de Fuentenueva, Edificio Mecenaz, Universidad de Granada, E-18071, Granada, Spain

²¹ Instituto Carlos I de Física Teórica y Computacional, Facultad de Ciencias, E-18071, Granada, Spain

²² Max-Planck-Institut für Extraterrestrische Physik (MPE), Giessenbachstraße 1, D-85748 Garching, Germany

²³ Space Telescope Science Institute, 3700 San Martin Drive, Baltimore, MD 21218, USA

²⁴ Kapteyn Astronomical Institute, University of Groningen, P.O. Box 800, 9700AV Groningen, The Netherlands

²⁵ DTU-Space, Technical University of Denmark, Elektrovej 327, 2800, Kgs. Lyngby, Denmark

²⁶ Center for Frontier Science, Chiba University, 1-33 Yayoi-cho, Inage-ku, Chiba 263-8522, Japan

²⁷ Department of Physics, Graduate School of Science, Chiba University, 1-33 Yayoi-Cho, Inage-Ku, Chiba 263-8522, Japan

²⁸ Steward Observatory, University of Arizona, 933 N. Cherry Avenue, Tucson, 85721, USA

Received 2023 November 6; revised 2024 January 18; accepted 2024 February 5; published 2024 April 11

Abstract

Sub/millimeter galaxies are a key population for the study of galaxy evolution because the majority of star formation at high redshifts occurred in galaxies deeply embedded in dust. To search for this population, we have performed an extensive survey with Atacama Large Millimeter/submillimeter Array (ALMA), called the ALMA Lensing Cluster Survey (ALCS). This survey covers 133 arcmin² area and securely detects 180 sources at $z \sim 0.5-6$ with a flux limit of ~ 0.2 mJy at 1.2 mm. Here, we report the results of multiwavelength spectral energy distribution analysis of the whole ALCS sample, utilizing the observed-frame UV to millimeter photometry. We find that the majority of the ALCS sources lie on the star-forming main sequence, with a smaller fraction showing intense starburst activities. The ALCS sample contains high infrared-excess sources ($\text{IRX} = \log(L_{\text{dust}}/L_{\text{UV}}) > 1$), including two extremely dust-obscured galaxies ($\text{IRX} > 5$). We also confirm that the ALCS sample probes a broader range in lower dust mass than conventional submillimeter galaxy samples in the same redshift range. We identify six heavily obscured active galactic nucleus (AGN) candidates that are not detected in the archival Chandra data in addition to the three X-ray AGNs reported by Uematsu et al. (2023). The inferred AGN luminosity density shows a possible excess at $z = 2-3$ compared with that determined from X-ray surveys below 10 keV.

Unified Astronomy Thesaurus concepts: [Submillimeter astronomy \(1647\)](#); [Galaxy evolution \(594\)](#); [High-redshift galaxies \(734\)](#); [Spectral energy distribution \(2129\)](#); [Active galactic nuclei \(16\)](#)

Supporting material: figure set

1. Introduction

The evolutionary scenario of galaxies and the supermassive black holes (SMBHs) at their centers is one of the most perplexing mysteries in modern astronomy. The tight bulge-

mass-to-SMBH-mass correlation in the local universe (e.g., Magorrian et al. 1998; Marconi & Hunt 2003; Kormendy & Ho 2013) suggests the coevolution of galaxies and SMBHs. This idea is also supported by the similarity between the cosmological evolution of star formation density and active galactic nucleus (AGN) luminosity density, which both reached a peak around $z \sim 2$ (Ueda et al. 2003; Madau & Dickinson 2014). However, the evolutionary scenario of an individual system is still unclear. High-redshift dusty star-forming galaxies (DSFGs) are a key population to elucidate the coevolution scenario, because the majority of star formation at high redshifts occurred in galaxies deeply enshrouded by dust.

Sub/millimeter observations are a powerful tool to study DSFGs in the high-redshift universe ($z \geq 3$). DSFGs are characterized by prominent far-infrared (FIR) emission from dust heated by stars. At high redshifts, the peak of dust emission is shifted to the sub/millimeter band, so that the sensitivity required to detect a galaxy with a given FIR luminosity is nearly constant across $z = 1-8$ in the millimeter band (Blain et al. 2002; Casey et al. 2014 for reviews). Hence, sub/millimeter observations can efficiently search for DSFGs in the high-redshift universe (often referred to as submillimeter galaxies, hereafter SMGs).

The Atacama Large Millimeter/submillimeter Array (ALMA) achieves excellent sensitivity and angular resolution in the millimeter band, and has been used to study SMGs. Here, we introduce some examples of representative ALMA surveys that are used as the comparison samples in this paper (see also Hodge & da Cunha 2020 for a recent review). The ALMA LABOCA E-CDFS Submillimeter Surveys (ALESS; Swinbank et al. 2012a, 2012b, 2014; Simpson et al. 2014; Hodge et al. 2013; Karim et al. 2013; Wang et al. 2013; Decarli et al. 2014; Thomson et al. 2014; Chen et al. 2015; da Cunha et al. 2015; Danielson et al. 2017) is an ALMA cycle 0 program to follow up ~ 100 SMGs that were previously detected by the single-dish LABOCA 870 μm survey in the extended Chandra Deep Field South (LESS; Weiß et al. 2009). It was able to separate unresolved multiple sources that were confused in the single-dish survey, and successfully yielded a reliable catalog of SMGs. In order to search for rare populations and to improve statistics, Stach et al. (2019) performed ALMA imaging follow-up of the SCUBA-2 UDS survey (AS2UDS) in cycles 1, 3, 4, and 5. This survey observed 716 SMGs in the UKIRT Infrared Deep Sky Survey Ultra Deep Survey (UDS) field that were previously detected by the SCUBA-2 Cosmology Legacy Survey (S2CLS; Geach et al. 2017), and yielded the largest homogeneously selected SMG sample to date (see also Cooke et al. 2018; Stach et al. 2018; Gullberg et al. 2019; Algera et al. 2020; Dudzevičiūtė et al. 2020; Koprowski et al. 2020; Smail et al. 2021). To search for fainter (hence more numerous) sources, Dunlop et al. (2017) performed an ALMA deep survey in the GOODS-S/Hubble Ultra Deep Field (HUDF; Beckwith et al. 2006). It covered an area of ~ 4.5 arcmin² and detected 16 secure sources with a flux limit of 0.12 mJy at 1.3 mm. The ALMA twenty-Six Arcmin² survey of GOODS-S At One-millimeter (ASAGAO; Fujimoto et al. 2018; Hatsukade et al. 2018; Ueda et al. 2018; Yamaguchi et al. 2019, 2020) was designed to fill the gap between the ALESS and HUDF surveys in the area versus sensitivity space. The ASAGAO survey covered an area of 26 arcmin² and detected 25 sources at $\geq 5.0\sigma$ and 45 sources at $\geq 4.5\sigma$ (1.2 mm). We note that the GOODS-S area is also covered by an extensive survey at 1.1 mm called

GOODS-ALMA (Franco et al. 2018, 2020a, 2020b; Zhou et al. 2020; Gómez-Guijarro et al. 2022a, 2022b; Ciesla et al. 2023). To simultaneously search for blank-field CO line and dust continuum, the large program called ALMA Spectroscopic Survey in the HUDF (ASPECS) was performed in cycle 4 (Aravena et al. 2016a, 2016b, 2019, 2020; Decarli et al. 2016a, 2016b, 2019, 2020; Bouwens et al. 2016; Carilli et al. 2016; Walter et al. 2016; Boogaard et al. 2019; Popping et al. 2019; Uzgil et al. 2019; Boogaard et al. 2020; González-López et al. 2020; Inami et al. 2020; Magnelli et al. 2020; Popping et al. 2020; Uzgil et al. 2021). This survey covered ~ 4 arcmin² and detected 35 secure sources with a flux limit of ~ 0.04 mJy at 1.2 mm.

In ALMA cycle 6, our team performed a large survey in 33 lensing clusters called ALMA Lensing Cluster Survey (ALCS; Caputi et al. 2021; Fujimoto et al. 2021, 2023; Jolly et al. 2021; Laporte et al. 2021; Kokorev et al. 2022; Sun et al. 2022; Kohno et al. 2023; Uematsu et al. 2023), in order to detect faint sources by utilizing the lensing effect. The ALMA observations were designed to target areas that were covered by the major Hubble Space Telescope (HST) treasury programs: Cluster Lensing And Supernova Survey with Hubble (CLASH; Postman et al. 2012), Hubble Frontier Fields (HFFs; Lotz et al. 2017), Beyond Ultra-deep Frontier Fields And Legacy Observations (BUFFALO; Steinhardt et al. 2020), and Reionization Lensing Cluster Survey (RELICS; Coe et al. 2019). The total area covered is 133 arcmin² (primary beam sensitivity in the mosaic maps of $>30\%$), with 180 sources securely detected down to an image-plane flux limit of ~ 0.2 mJy at 1.2 mm and a source plane flux limit of ~ 7 μJy , which is one of the deepest surveys after lensing correction (see Section 2.1 for details).

In this paper, we report the results of multicomponent spectral energy distribution (SED) analysis for the whole ALCS sample, utilizing the UV-to-millimeter photometry obtained by ALMA, HST, Spitzer Space Telescope (Spitzer), and Herschel Space Observatory (Herschel). In Section 2, we summarize the observations and data reduction. In Section 3, we explain the SED analysis and comparison samples. In Section 4, we show the results of the SED analysis. In Section 5, we discuss the dust properties and the nature of AGNs in our sample. Finally, we provide a summary and conclusions in Section 6. Throughout the paper, we assume a flat universe with $H_0 = 70.4$ km s⁻¹ Mpc⁻¹, and $\Omega_M = 0.272$ (Komatsu et al. 2011). The Chabrier initial mass function (IMF; Chabrier 2003) is adopted. If not specifically mentioned, errors correspond to 1σ confidence.

2. Observations and Data Reduction

2.1. Observations and Source Detection with ALMA

The 1.2 mm continuum source catalog was built by Fujimoto et al. (2023). Here, we briefly explain the observations and the data reduction. The ALCS fields were observed in ALMA Band 6 between 2018 and 2019 December through the program 2018.1.00035.L (PI: K. Kohno; Kohno et al. 2023). These observations covered 250.0–257.5 GHz and 265.0–272.5 GHz with a total bandwidth of 15 GHz. The synthesized beam size is $\sim 1''$. All the ALMA data were calibrated and reduced with the Common Astronomy Software Applications package (CASA). The existing ALMA data from 2013.1.00999S to 2015.1.01425.S (PI: Bauer; González-López et al. 2017) were

also combined for five Hubble Frontier Fields. The source detection was performed with the `SETRACTOR` in native (full width at half-maximum, $\text{FWHM} \sim 1''$) and tapered maps ($\text{FWHM} \sim 2''$) with natural weighting. First, in a blind search, 141 sources were detected with a signal-to-noise ratio (S/N) over 5.0 in the natural maps or over 4.5 in the tapered maps, which corresponds to a false-detection rate of $< 1\%$. Second, in a prior-based approach, 39 sources are detected with $5.0 \geq \text{S/N} \geq 4.0$ (a false-detection rate of $< 50\%$) in the natural maps associated with Spitzer/IRAC channel 2 ($4.5 \mu\text{m}$) detection ($\text{S/N} \geq 5.0$). Hereafter, we refer to the former as the MAIN sample and the latter as the SECONDARY sample.

2.2. HST, Spitzer, and Herschel Counterparts

The ALCS fields were observed with HST, Spitzer, and Herschel previously. The images and photometric catalogs of optical and near-infrared bands were built by Kokorev et al. (2022) by reprocessing the best-available archival data from HST and Spitzer/IRAC channels 1 and 2. Sun et al. (2022) produced the FIR images and catalogs, utilizing the best-available data of Herschel/PACS and SPIRE. The quality of the multiwavelength photometry is summarized in Section 2.4. We note that the photometric data of Spitzer/IRAC channel 2 are sometimes inconsistent with the other photometries, which may be due to remaining blending effects or oversubtraction of nearby sources. For this reason, the photometric data of Spitzer/IRAC channel 2 in M0416-ID120, M1206-ID60, ACT0102-ID11, M1115-ID34, and ACT0102-ID224 are not used in the SED modeling.²⁹

In addition to these catalogs, we utilize the photometric data of Spitzer/IRAC channels 3 ($5.8 \mu\text{m}$) and 4 ($8.0 \mu\text{m}$), and those of Spitzer/MIPS channel 1 ($24 \mu\text{m}$), taken from the Spitzer Enhanced Imaging Products (SEIP; SSC and IRSA 2020). Those sources are cross-matched with the ALMA source positions within $1''.5$. Since IRAC and MIPS have large beam sizes (full width at half-maximum of $1''.8$, $1''.9$, and $5''.9$ at 5.8 , 8.0 , and $24 \mu\text{m}$, respectively), the measured photometric data can be contaminated by nearby sources. To evaluate this effect, we compare the flux densities of IRAC channel 2 extracted from the SEIP (f_{SEIP}) with those in the catalog by Kokorev et al. (2022) (f_{ALCS}), who deblended the photometric data utilizing the HST source positions. If $0.5 < f_{\text{ALCS}}/f_{\text{SEIP}} < 2.0$, we use the photometric data from the SEIP for our SED modeling. If $f_{\text{ALCS}}/f_{\text{SEIP}} < 0.5$, we treat the SEIP data as upper limits. In the case of $f_{\text{ALCS}}/f_{\text{SEIP}} > 2.0$, we conservatively do not utilize the data from the SEIP, considering the possibility of mismatching with the ALMA source.

2.3. Chandra Observations

Uematsu et al. (2023) detected three AGNs among the lensed ALCS sources, utilizing the archived data of Chandra; hereafter, we refer to these AGNs as ‘‘ALCS-XAGNs.’’ In this paper, we derive the 3σ upper bounds³⁰ of the X-ray luminosities for the rest of the sources. First, we reprocessed all the data obtained with Chandra by 2021, following the standard procedures with the Chandra interactive analysis of observations software (CIAO v4.12) and the calibration database (CALDB v4.9.1).

²⁹ We note that these sources were not detected in the Spitzer/IRAC channel 3, 4; and Spitzer/MIPS channel 1 in the SEIP catalog.

³⁰ In this paper, we refer to the upper edge of a confidence interval as ‘‘upperbound’’ (see Kashyap et al. 2010 for more details).

Table 1
Classification of the ALCS Sources

Tier (1)	HST (2)	Spitzer (3)	Herschel (4)	N (5)
1	✓	✓	✓	99 (79)
2	✓	✓	...	28 (16)
3	...	✓	✓	21 (20)
4	...	✓	...	10 (7)
5	✓	...	✓	3 (3)
6	✓	1 (0)
7	✓	2 (2)
8	2 (2)

Note. (1) Class. (2)–(4) The quality of the data. If a source is detected above 2σ in at least one band, the corresponding column is checked by the symbol (✓). (5) The number of ALCS sources that meet the criteria. The number in parentheses shows the number of sources that belong to the MAIN sample. In this classification, BCGs (11 sources), a possible mismatched source, a possible contaminated source, and a spectroscopically confirmed member galaxy of a cluster are excluded. The multiply imaged sources are counted individually.

Next, we combined the products by using `merge_obs`. Then, we ran `srcflux` to the combined data and obtained the 3σ upper bounds of the 0.5–7 keV count rates for each source. For the source and background regions, we employed circular regions with radii of $1''.5$ and annuli with inner and outer radii of $2''$ and $4''$, respectively, after masking obvious X-ray point sources. Then, we converted the count rates to the intrinsic X-ray luminosities, assuming typical X-ray spectra of AGNs. Since there are no Chandra observations in RXC0032 and RXC0600, the X-ray luminosity upper bounds in those fields are not given. We excluded the brightest cluster galaxies (BCGs) from the catalog because of the difficulty in separating the X-ray point sources from the diffuse X-ray emission of the galaxy clusters. Details of the X-ray spectral models and the results are summarized in Appendix A.

2.4. Data Quality, Sample Selection, and Magnification

We classify the ALCS sources into eight groups based on the quality of the multiwavelength photometry. The criteria are summarized in Table 1. In this classification, BCGs (11 sources³¹; A383-ID40, M0159-ID46, M0429-ID19, M1115-ID36, M1206-ID58, M1423-ID50, M1931-ID41/42, R0032-ID162, R1347-ID75, R2129-ID20), a possible mismatched source (R0600-ID67), and a possible contaminated source (R0600-ID164) are excluded. A370-ID31 is also excluded because it is spectroscopically confirmed as a member galaxy of the foreground cluster (A370). We note that this classification is independent of the one that is based on the source detection (either blind [MAIN] or prior-based [SECONDARY]) in the ALMA band (see Section 2.1).

The magnification factors are extracted from Fujimoto et al. (2023), where the lens model of GLAFIC (Oguri 2010) is adopted as a fiducial. Figure 1 shows the histogram of the magnification factors in the tier-1/2/3/4/5/6 samples. Here, we note that the uncertainties in the lens models and magnification factors are not considered in this paper. Such uncertainties can affect the physical quantities of each source; however, they do not change the qualitative discussion. We spectroscopically confirm six multiply imaged sources

³¹ We follow the classification in Sun et al. (2022).

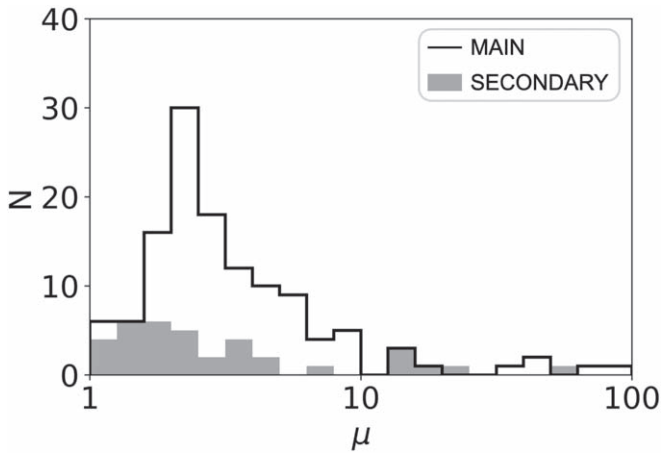


Figure 1. Distribution of the magnification factor in the ALCS tier-1/2/3/4/5/6 samples. One source belonging to the SECONDARY sample lies off the plot with $\mu = 0.15$ ($z = 0.63 \pm 0.10$). The multiply imaged sources are counted individually.

(ACT0102-ID118/215/224; $z = 4.32$, MACS0417-ID46/58/121; $z = 3.65$, MACS0553-ID133/190/249; $z = 1.14$, M1206-ID27/55/60/61; $z = 1.04$, R0032-ID32/53/55/57/58; $z = 3.63$, R0032-ID208/281/304; $z = 2.98$). We also regard R0032-ID127/131/198 and ACT0102-ID223/294 as multiple images of single sources at $z = 2.391$, and $z = 4.0 \pm 0.5$, based on the source positions, the lens models, and the similarities in their SEDs. Moreover, A2537-ID24/66 and R0032-ID63/81 are also treated as multiple images at $z = 3.2$, and $z = 3.0$, which are used to construct the lens models in the literature (see Fujimoto et al. 2023 for details).

3. Analysis

3.1. SED Modeling with CIGALE

We conduct multicomponent SED modeling to the UV to millimeter photometry of the ALCS tier-1/2/3/4/5/6 samples, except for the three ALCS-XAGNs, whose SEDs are already analyzed by Uematsu et al. (2023). The tier-7/8 samples are not analyzed in this paper because it is challenging to derive the physical properties from their limited photometric data. Although these sources are located within the coverages of HST and Spitzer, they are too faint to be detected with these observatories. This suggests that those sources are heavily obscured galaxies in the high-redshift universe. We use the Code Investigating GALaxy Emission (CIGALE; Boquien et al. 2019; Yang et al. 2022), incorporating modifications to the dust emission model. CIGALE assumes an energy balance between UV/optical absorption and infrared reemission, which enables us to self-consistently model the SED of each galaxy. Moreover, CIGALE can simultaneously treat AGN and galaxy components, which enables us to assess the contribution of AGN in the SED.

The SED modules assumed in this study are described in the following subsections. The free parameters are summarized in Appendix B. In the SED modeling, the multiply imaged sources are treated individually. The redshifts are fixed at the values reported in Fujimoto et al. (2023; 69/180 sources have spectroscopic redshifts). The uncertainties of the photometric redshifts are not considered in the main part of this paper. The redshift uncertainties and their impact on the estimation of the physical properties are discussed in Appendix C, where we

treat photometric redshifts utilizing MAGPHYS (da Cunha et al. 2008, 2015; Battisti et al. 2019, 2020).

3.1.1. Stellar Emission, Dust Attenuation, and Nebular Emission

In our CIGALE SED modeling, we employ a delayed star formation history (SFH), assuming an additional burst with exponential decay. The simple stellar population (SSP) is modeled with the stellar templates of Bruzual & Charlot (2003), assuming the Chabrier (2003) IMF. The dust attenuation is modeled with the Calzetti starburst attenuation law (Calzetti et al. 2000), where we allow slightly steeper or flatter curves than the original one (see Appendix B for the parameter range). We also add nebulae emission according to Inoue (2011).

3.1.2. AGN Emission

We employ the Skirtor model (Stalevski et al. 2012, 2016) for the optical and infrared emission from an AGN. The Skirtor model assumes anisotropic radiation from an accretion disk and a dusty torus composed of two-phase matter. We also add a polar dust emission modeled by a single graybody, where we assume an emissivity index of 1.6, temperature of 150 K, and opacity of unity at 200 μm . To identify whether a galaxy hosts an AGN or not, we utilize the Bayesian Information Criterion (BIC; Schwarz 1978). The BIC is calculated as $\text{BIC} = \chi^2 + k \times \ln(n)$, where χ^2 is the non-reduced chi-square, k is the number of degrees of freedom (dof), and n is the number of the photometric data points. If the addition of an AGN component reduces BIC by more than 10 ($\Delta\text{BIC} = \text{BIC}_{\text{noAGN}} - \text{BIC}_{\text{AGN}} > 10$), we consider that the AGN component is needed for the SED (see Toba et al. 2020). For the tier-2/3/4/5/6 samples, the AGN component is always excluded, because it is challenging to identify the presence of an AGN from the limited photometry of those samples.

3.1.3. Dust Emission from Host Galaxy

Recent studies have shown that some SMGs and local Ultra Luminous Infrared Galaxies (ULIRGs) exhibit higher dust temperatures compared to typical local galaxies (Cortese et al. 2014; Clements et al. 2018; da Cunha et al. 2021). Currently, the physically based dust emission models implemented in CIGALE cannot properly account for these populations due to the limited range of dust temperatures. This limitation in the higher temperature regimes may result in an overestimation of AGN contribution, particularly that of polar dust emission from the AGN, or an underestimation of infrared luminosity from star formation activity. Therefore, we develop a new dust emission model by extending the parameter range of the Themis model (Jones et al. 2017), which is the latest dust-emission model implemented in CIGALE.

We use the DustEM code (Compiègne et al. 2011) to extend the Themis model. Dust temperature is characterized by the minimum radiation field illuminating the interstellar dust (U_{min}). In the current version of the Themis model, U_{min} is limited to 0.1–80, which corresponds to 12–39 K.³² We extend it to $U_{\text{min}} = 0.1\text{--}6309(10^{-1}\text{--}10^{3.8})$ with a step size of 0.2 in logarithmic space. This parameter range corresponds to $T_{\text{dust}} = 12\text{--}83$ K ($T_{\text{dust}}^{\text{peak}} = 20\text{--}141$ K; see Section 3.3), which is almost equivalent to the likelihood distribution of dust temperature in the ALESS sample (20–80 K;

³² Here, we use T_{dust} to refer to the intrinsic temperature of interstellar dust illuminated with $U = U_{\text{min}}$ ($T_{\text{dust}} = 18.3 U_{\text{min}}^{1/5.79}$ K; Nersesian et al. 2019).

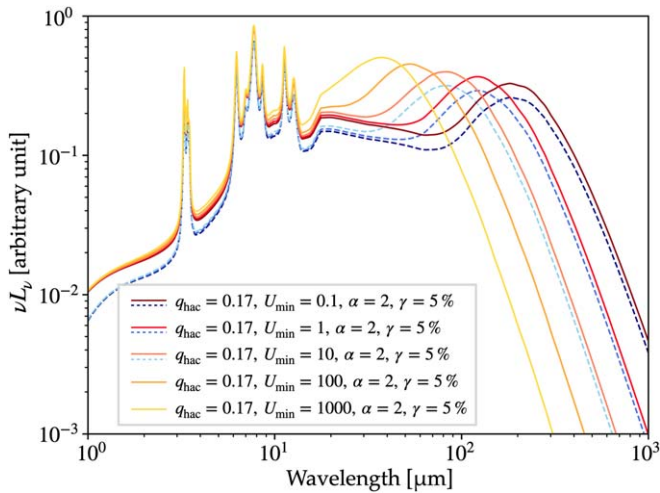


Figure 2. Example of SEDs in the Themis (dashed lines) and the EThemis model (solid lines) spanning a wide range in dust temperature. All the SEDs in this figure are normalized by the total luminosity, while a small systematic offset is imposed in the Themis model to improve visibility.

da Cunha et al. 2015). We confirm that the extended model successfully reproduces the original Themis model by covering high dust temperature cases. Figure 2 compares the original Themis model and our new model, which we hereafter call EThemis (Extended Themis).

3.2. Estimation of Physical Properties

For the estimation of physical properties, we calculate the likelihood-weighted mean of all the models on the grid as a Bayesian estimation, where we treat the following parameters in a logarithmic space:

1. star formation rate (SFR),³³
2. stellar mass (M_*),
3. dust luminosity (L_{dust}) and mass (M_{dust}).³⁴

Meanwhile, the following parameters are treated in a linear space:

1. dust temperature (T_{dust}),
2. color excess of stellar continuum attenuation ($E(B - V)$),
3. infrared excess ($\text{IRX} = \log(L_{\text{dust}}/L_{\text{UV}})$),
4. power-law index of observed UV slope (β),³⁵
5. power-law index to modify the attenuation slope (δ),³⁶
6. bolometric AGN luminosity ($L_{\text{AGN,bol}}$).

This means that we calculate the likelihood-weighted mean of the marginalized PDF with a log-uniform prior for the former parameters and with a uniform prior for the latter, respectively. The specific star formation rates (sSFR = SFR/stellar mass) are derived from the stellar masses and the SFRs, where the confidence intervals of the sSFRs are calculated by propagating the uncertainties associated with the stellar masses and the SFRs. We correct all the quantitative variables for the lensing effect by dividing the observed values by the magnification factors.

³³ In this paper, the term *SFR* refers to the average SFR in the last 10 Myr.

³⁴ In this paper, we use the terms *dust luminosity* and *dust mass* to describe those of interstellar dust (i.e., not including those in the AGN torus).

³⁵ The power-law index of observed UV slope is measured in the same way as that in Calzetti et al. (1994).

³⁶ The definition of δ is described in Equation (8) in Boquien et al. (2019).

3.3. Characteristic Dust Temperature

The definition of the term *dust temperature* varies from study to study. For example, Nersesian et al. (2019) employ the term to denote the intrinsic temperature of interstellar dust illuminated by the minimum radiation field ($U = U_{\text{min}}$), which is the same definition employed in our EThemis model. By contrast, Sun et al. (2022) define the term as the luminosity-weighted average of the intrinsic temperature of two optically thin graybodies. Furthermore, the measured dust temperature is also highly dependent on the assumptions of models, e.g., the assumption of dust opacity (Casey 2012; Dudzevičiūtė et al. 2020; da Cunha et al. 2021). Therefore, to properly compare different studies, the dust temperature in each study should be converted according to a common definition. One way is to use the inverse *peak wavelength* temperature ($T_{\text{dust}}^{\text{peak}}$), which is calculated from the peak wavelength of the FIR dust emission using the Wien's displacement law³⁷:

$$T_{\text{dust}}^{\text{peak}} [\text{K}] = 5099 / \lambda^{\text{peak}} [\mu\text{m}]. \quad (1)$$

Since this value directly reflects the shape of the dust SED, it is less affected by the assumptions of models and hence is useful for comparing different studies. Therefore, we use the inverse peak-wavelength temperature to compare different samples; hereafter, we refer to this temperature as *characteristic dust temperature*. However, it should be noted here that the characteristic dust temperature does not denote the intrinsic temperature of dust, and one should be careful when interpreting this value.

3.4. Comparison Samples

We discuss our results in comparison with previous ALMA surveys (e.g., ASAGAO, ASPECS, ALESS, AS2UDS, and ALPINE). The flux densities and the redshifts of the ASAGAO, ASPECS, ALESS, and AS2UDS samples are extracted from Hodge et al. (2013), Aravena et al. (2020), Yamaguchi et al. (2020), and Dudzevičiūtė et al. (2020), respectively. The other physical properties discussed in this paper are taken from da Cunha et al. (2015), Aravena et al. (2020), Yamaguchi et al. (2020), and Dudzevičiūtė et al. (2020), respectively. We also utilize the results from da Cunha et al. (2021), which discussed the dust properties of the well-sampled subset of the ALESS sample utilizing a 2 mm observation with ALMA. In addition, the physical properties of the ALPINE sample are extracted from Boquien et al. (2022).

Figure 3 shows the histograms of 1.2 mm flux densities.³⁸ We confirm that the ALCS basically fills the gap between ALESS/AS2UDS and ASPECS, although the ALCS detects especially faint sources that were not detected in the previous surveys thanks to the lensing effect. The right panel of Figure 3 shows the histograms of redshifts. We see that the ALCS sample contains mainly high-redshift ($z > 1$) galaxies like the other sub/millimeter selected samples (ALESS, ASAGAO, ASPECS, AS2UDS), reflecting the effect of negative *K*-correction.

The SEDs of the ALESS, ASAGAO, ASPECS, and AS2UDS samples were analyzed with MAGPHYS

³⁷ Since FIR photometry is often given in the dimension of Jy , we utilize the peak wavelength in the dimension of Jy ($\text{erg s}^{-1} \text{cm}^{-2} \text{Hz}^{-1}$) to calculate the characteristic dust temperature.

³⁸ The flux densities of the ALESS and AS2UDS samples are converted from those at 870 μm , assuming an optically thin graybody with an emissivity index of 1.8 and an intrinsic temperature of 35 K (e.g., Coppin et al. 2008; Planck Collaboration et al. 2011).

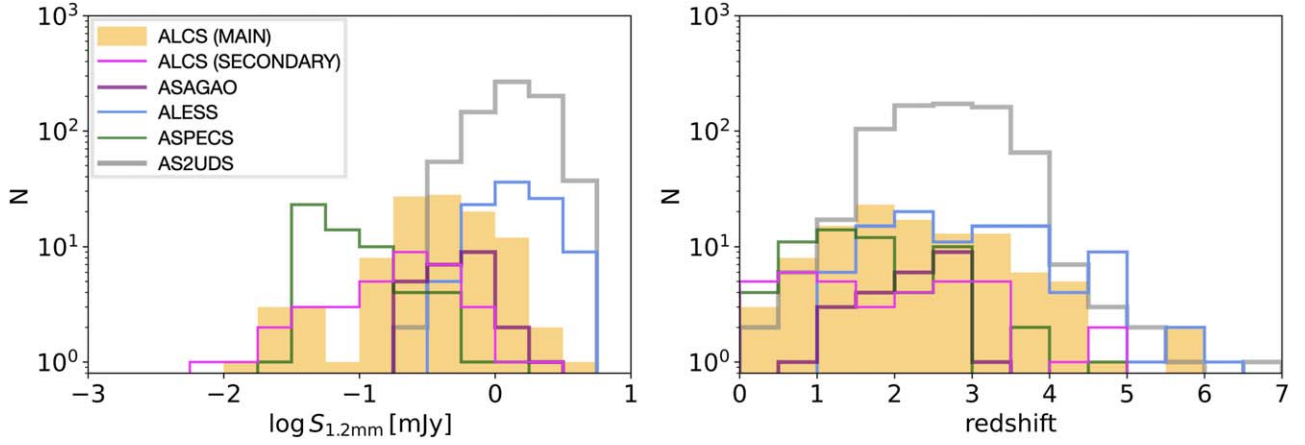


Figure 3. Left: flux–density distribution of sources detected in major ALMA surveys. Right: their redshift distribution. In these histograms, only the ALCS tier-1/2/3/4/5/6 samples are counted for the ALCS sample. For each set of multiple images, we include only one image, which is selected with priorities given to a higher tier sample and to an image with a smaller magnification factor. The flux densities of the ALCS sources are corrected for lensing magnification.

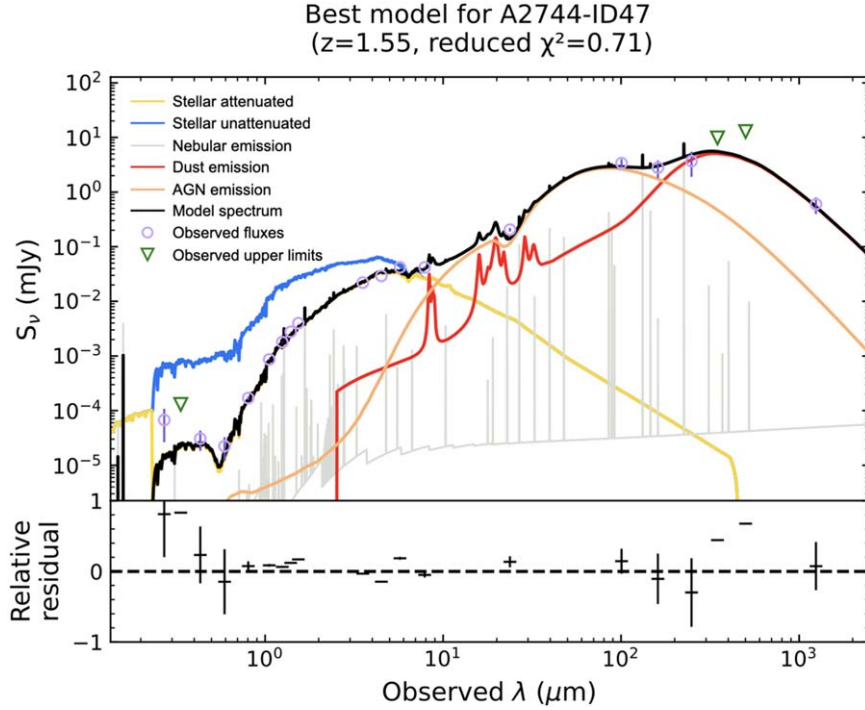


Figure 4. The SED and the best-fit model of A2744-ID47. Lensing magnification is NOT corrected in this figure. The black solid line represents the composite spectrum of the galaxy. The yellow line illustrates the stellar emission attenuated by interstellar dust. The blue line depicts the unattenuated stellar emission for reference purposes. The orange line corresponds to the emission from an AGN. The red line shows the infrared emission from interstellar dust. The gray line denotes the nebulae emission. The observed data points are represented by purple circles, accompanied by 1σ error bars. The bottom panel displays the relative residuals.

(da Cunha et al. 2008, 2015), while those of the ALPINE and ALCS samples are analyzed with CIGALE. To check the systematic difference between these codes, we also analyze the SEDs of the ALCS sample with MAGPHYS. The results are summarized in Appendix D. Accordingly, we impose a systematic offset of -0.37 dex in the stellar mass of the AS2UDS, ASAGAO, ALESS, and ASPECS samples. The SFRs, dust luminosities, and dust masses are not corrected, because we did not find obvious systematic differences for these parameters. Moreover, we use the characteristic dust temperature to compare the dust temperature among different studies. The conversion methods of dust temperature among different definitions are summarized in Appendix E.

4. Results

We successfully reproduce the SEDs of the ALCS tier-1/2/3/4/5/6 samples with a fit quality of $\chi^2/\text{dof} < 5$. Figure 4 shows the example SED of the ALCS sample. The fit quality is shown in Figure 5. All the SEDs and the best-fit models are summarized in Appendix B.

4.1. Overall Properties of ALCS Sample

Figure 6 shows the distribution of the ALCS sample across nine parameter spaces. We confirm that the MAIN sample comprises galaxies with higher dust luminosities, dust mass, and SFRs. We also confirm that the SECONDARY sample tends to

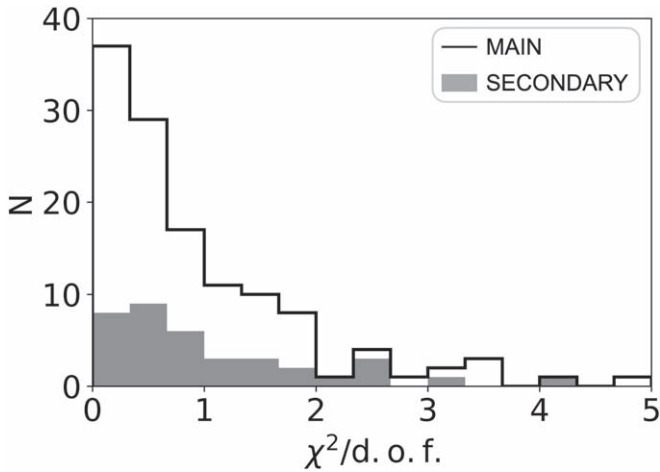


Figure 5. Histogram of fit quality of the ALCS tier-1/2/3/4/5/6 samples. The multiply imaged sources are counted individually.

contain galaxies with lower $E(B - V)$ and lower IRX. These differences can be explained by the selection effects. Since the MAIN sample is selected by higher significance in the ALMA band, it contains galaxies that are brighter in the millimeter band. This results in the higher dust luminosities, dust mass, and SFRs of the MAIN sample. By contrast, since the IRAC/ch2 band can suffer from dust attenuation in the high-redshift universe, the IRAC selection of the SECONDARY sample might cause a selection bias against heavily attenuated sources.

Adhering to the methodology outlined in Section 3.1.2, we identify six AGN candidates within the tier-1 sample (excluding ALCS-XAGNs); hereafter, we refer to these AGN candidates as *ALCS-nonXAGNs*. Figure 7 shows the histogram of ΔBIC . Here, we note that R0032-ID57 is also classified as an AGN with the BIC selection ($\Delta\text{BIC} = 13.3$). However, the other multiple images (R0032-ID32/53/55/58) are not classified as AGNs, and no obvious signs of AGN are found in the SED of R0032-ID57. Therefore, we do not consider R0032-ID57 as a host of an AGN.

4.2. SFR versus Stellar Mass

Figure 8 plots the relation between stellar mass and SFR. For comparison, we plot the star-forming “main sequence” given by Schreiber et al. (2015). This figure shows that the majority of the ALCS sources are in the star-forming main sequence (82/162 [51%] sources are in the ranges 4 times above or below the star-forming main sequence), while some of them show intense starburst activities (69/162 [43%]), and the others (11/162 [7%]) are below the main sequence. This trend is similar to what is seen for the ALESS, AS2UDS, and ASAGAO samples, although the ALCS sample contains sources with even lower SFRs and stellar masses. On the other hand, the ALCS sample shows higher SFRs compared to the ASPECS sample. These differences simply reflect the different sample selections. Since the effective depth of ALCS is deeper than those of ALESS, AS2UDS, and ASAGAO due to the lensing effect, ALCS was able to detect galaxies with lower SFRs (M_* is typically lower, according to the star-forming main sequence). At the same time, because the survey area with strong-lensing effects is limited, the ALCS sample generally has higher SFRs compared with ASPECS, which is a homogeneously deep survey with ALMA.

4.3. IRX versus Stellar Mass

The left panel of Figure 9 shows the relation between stellar mass and IRX. For comparison, we plot the conventional relationship of optical or UV selected galaxies at $z \sim 2-3$ studied by Reddy et al. (2010), Whitaker et al. (2014), and Álvarez-Márquez et al. (2016), as compiled by Bouwens et al. (2016). We see that the ALCS sample has higher IRXs than the conventional relationship, implying that these galaxies are more deeply enshrouded by dust than optical- or UV-selected galaxies. We also find two extremely dusty-obscured galaxies that have especially high IRX (A2744-ID7 [IRX = 6.3 ± 0.8] and R0600-ID111 [IRX = 5.6 ± 0.6]). Figure 10 shows the SEDs of the two sources. These galaxies have steeper attenuation curves than the average (the steepness of the attenuation slopes are -1.0 ± 0.2 and -0.8 ± 0.1 , respectively), which may result in more UV absorption and thus larger IRX. Recently, Kokorev et al. (2023) found a potential major merger at $z = 2.58$ that is deeply enshrouded by dust utilizing James Webb Space Telescope (JWST) observations. This might suggest that high-IRX sources in SMG samples are important targets for JWST to reveal the evolutionary stages of distant galaxies and SMBHs. We note that there still remain some sources that potentially have high IRXs (R0032-ID281 [6.3 ± 1.8], ACT0102-ID22 [6.0 ± 1.6], A3192-ID131 [5.8 ± 1.5], R0032-ID245 [5.7 ± 1.5], and R0949-ID14 [5.5 ± 1.7]), which belong to the tier-3/4 samples. Moreover, the tier-7/8 samples may also contain such a population, although they are not analyzed in this study. Deeper observations in optical and near-infrared bands are needed to confirm the nature of these sources.

4.4. IRX versus Observed UV Slope

The right panel of Figure 9 shows the relation between IRX and observed UV slope. For comparison, we plot the local relation derived by Takeuchi et al. (2012) and the so-called SMC IRX- β relation, which is based on the observational results of Lequeux et al. (1982), Prevot et al. (1984), and Bouchet et al. (1985; see also Pei 1992; Pettini et al. 1998; Smit et al. 2016). The color map shows the steepness of the attenuation slopes. We see that the ALCS sample is distributed above the local relation at $\beta \lesssim 3$, while it is close to the SMC IRX- β relation at $\beta \gtrsim 3$. This can be explained by the sample selection. Since the ALCS sample is selected by millimeter observations, it is more sensitive to high-IRX sources than UV/optical selected samples. On the other hand, since the tier-1/2/3/4/5/6 samples are also selected by HST or IRAC observations, those samples miss the sources that have both high IRX and small β , which are faint even in the near-infrared band.

We also confirm a large scatter in the steepness of attenuation slopes, which strongly affects the IRX- β relation, i.e., galaxies with flatter attenuation slopes (high δ) tend to show bluer UV spectrum (low β). As will be discussed in Section 5.1.1, the steepness of the attenuation slope is weakly correlated with the stellar mass. This might account for the differences in the IRX- β relation for different stellar masses reported in recent studies (e.g., Bouwens et al. 2020). However, the IRX- β relation can also be strongly affected by the geometry of dust and stellar components (e.g., Popping et al. 2017; Narayanan et al. 2018; Fudamoto et al. 2020). A spatially resolved SED analysis with high-resolution observation will be helpful to reveal the dust properties in high-redshift star-forming galaxies.

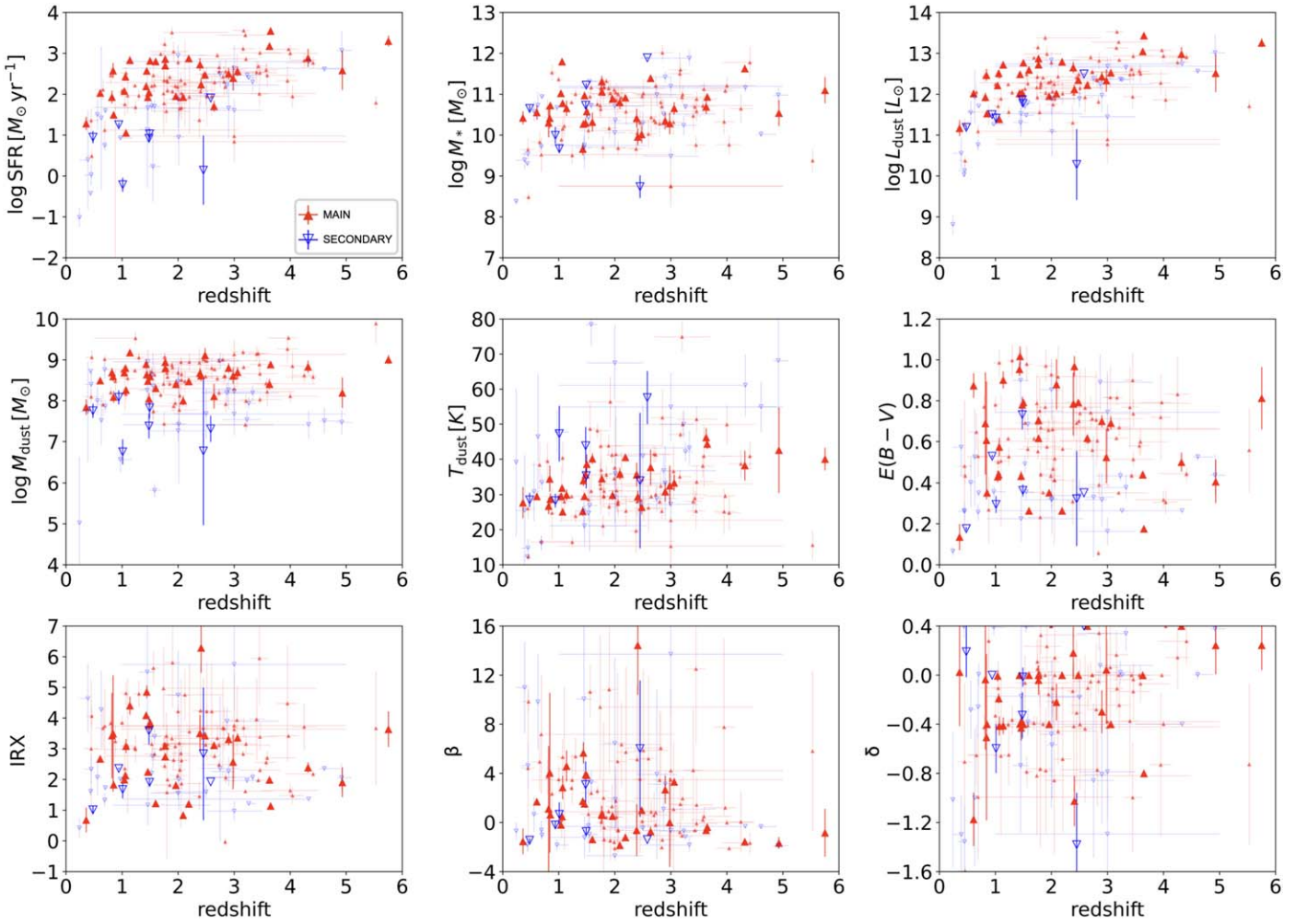


Figure 6. Distribution of the ALCS tier-1/2/3/4/5/6 samples in nine parameter spaces. The physical properties of ALCS-XAGNs are extracted from Uematsu et al. (2023). The filled red triangles represent the MAIN sample, and the blue open triangles the SECONDARY sample. The large symbols show the galaxies that have spectroscopic redshifts, while the small symbols show those with photometric redshifts. For each set of multiple images, we include only one image, which is selected with a priority given to a higher tier sample and to an image with a smaller magnification factor, whose uncertainty is expected to be smaller. All the physical quantities in this figure are NOT corrected for lensing magnification.

5. Discussion

5.1. Dust Properties

In this subsection, we discuss the dust properties of the ALCS sample. We focus on the dust attenuation law, dust temperature, and dust mass.

5.1.1. Dust Attenuation Law

The dust attenuation law is critical to study the stellar populations and thus the evolutionary scenario of galaxies. Over time, numerical studies have revealed the extensive variation in attenuation curves among different galaxies and even within a single galaxy depending on the line of sight (e.g., Nandy et al. 1975, 1980; Rocca-Volmerange et al. 1981). The main features to characterize an attenuation curve are the steepness of the curve and the depth of the 2175 Å bump (UV bump). Unfortunately, it is challenging to measure the depth of UV bumps with the poor photometric data of high-redshift galaxies. Therefore, in this paper, we focus only on the steepness of the attenuation curves of the ALCS sample.

In the modified Calzetti starburst attenuation law, the steepness of the attenuation curve is quantified by δ , the

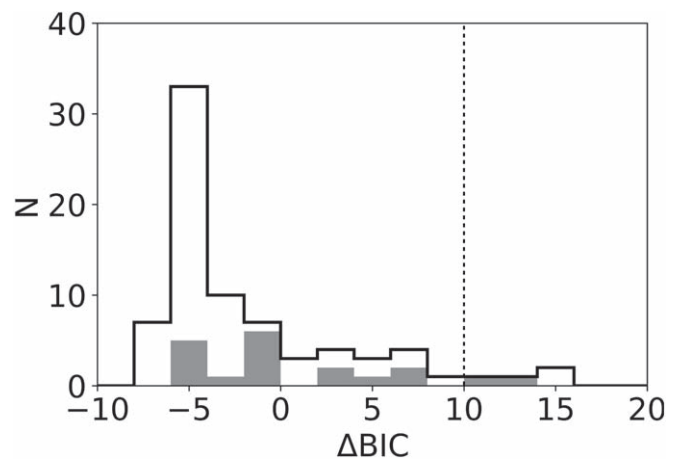


Figure 7. Distribution of ΔBIC in the ALCS tier-1 samples (ALCS-XAGNs are excluded). One source belonging to the SECONDARY sample lies off the plot with $\Delta\text{BIC} = 118$. The vertical dotted line shows $\Delta\text{BIC} = 10$. The multiply imaged sources are counted individually.

power-law index to modify the original Calzetti law (Calzetti et al. 2000). The left panel of Figure 11 gives a color-coded plot of δ on the sSFR versus stellar mass plane. We confirm

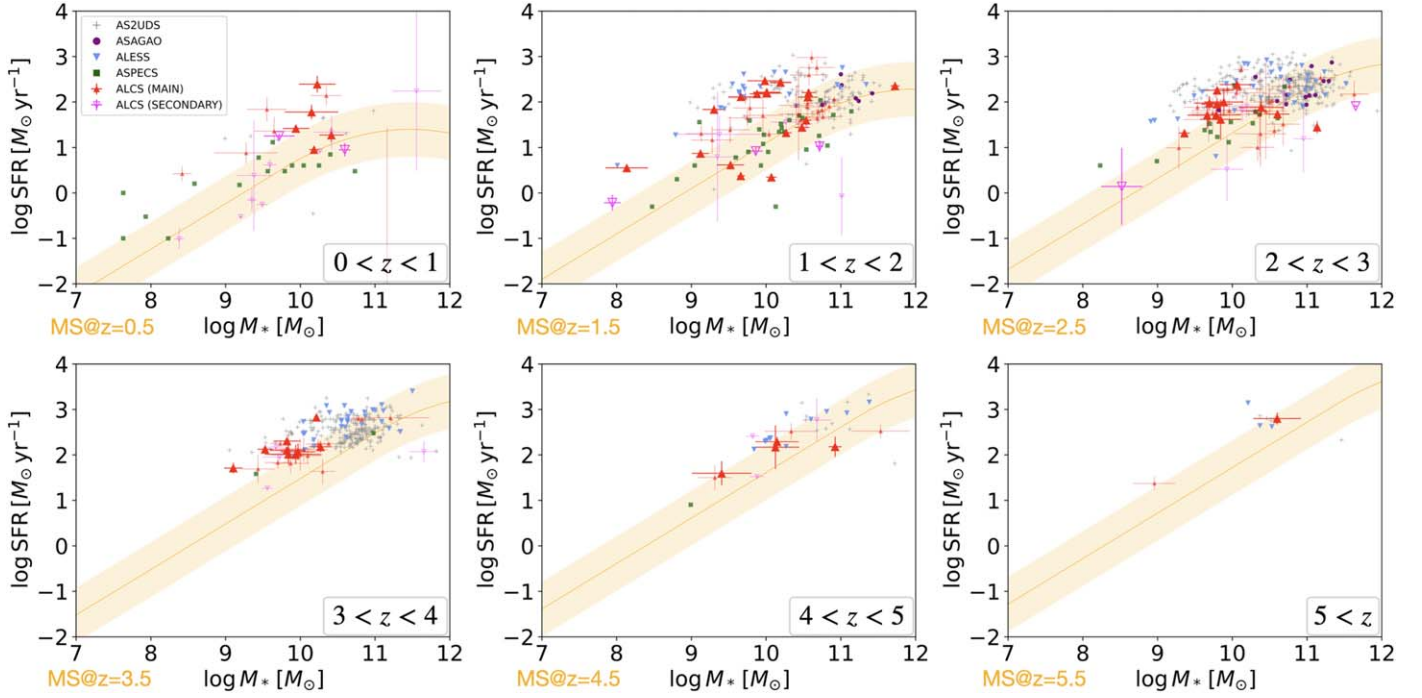


Figure 8. Relation between stellar mass (M_*) and SFR for galaxies detected in major ALMA surveys. The orange solid lines represent the star formation main sequence at each redshift (Schreiber et al. 2015). The light orange areas show the ranges 4 times above or below the main sequence. The large symbols show the galaxies with spectroscopic redshifts, while the small symbols show those with photometric redshifts. The multiply imaged sources are plotted individually. The stellar masses and the SFRs of the ALCS sources are corrected for lensing magnification.

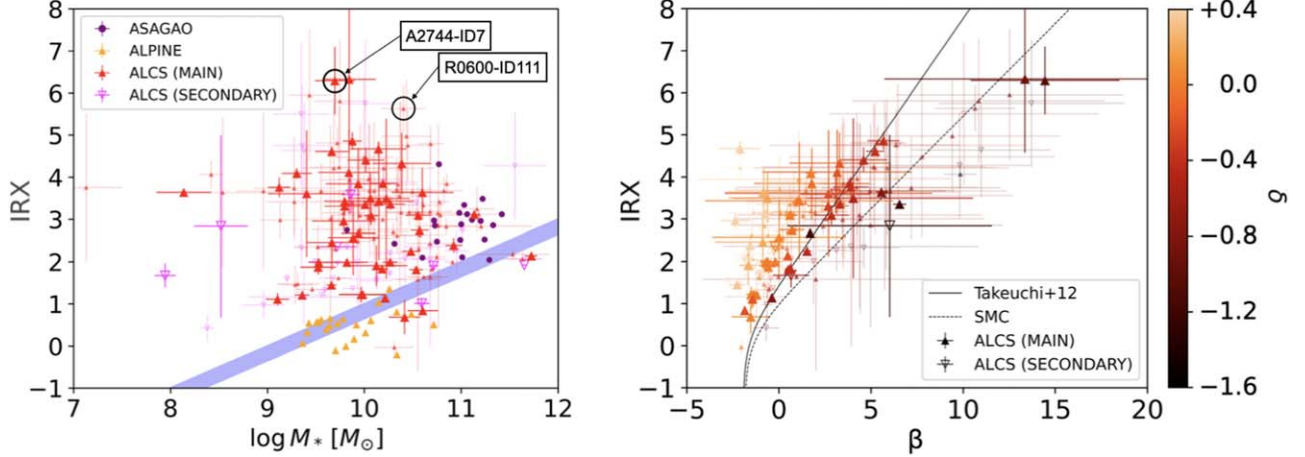


Figure 9. Left: Relation of IRX vs. stellar mass in major ALMA surveys. The blue line shows the conventional relation of optical or UV-selected galaxies at $z \sim 2-3$ compiled by Bouwens et al. (2016). Right: Relation of IRX vs. observed UV slope (β) in the ALCS sample. The color map shows the power-law index to modify the original Calzetti law (δ). The black solid and dashed lines show the local relationship derived by Takeuchi et al. (2012) and the so-called SMC IRX- β relationship, respectively. In these figures, the ALCS tier-1/2/3/4/5/6 samples are plotted. The large symbols show the galaxies with spectroscopic redshifts, while the small symbols show those with photometric redshifts. The multiply imaged sources are plotted individually. The stellar masses of the ALCS sources are corrected for lensing magnification.

that no strong correlation exists between δ and sSFR. The right panel of Figure 11 plots the relation between stellar mass and δ . A weak correlation is noticed between the steepness of attenuation curve and stellar mass, i.e., galaxies with high stellar masses tend to have flatter attenuation curves. This is consistent with the trend observed in local galaxies (Salim et al. 2018).

5.1.2. Dust Temperature

The cosmological evolution of dust temperature is a key issue for understanding star formation activity in the high-redshift

universe, as assumptions regarding dust temperature can significantly impact dust luminosity estimations and, consequently, SFRs. Some studies have claimed a global increase in dust temperature with redshift across $z = 0-9$ (see, Schreiber et al. 2018; Viero et al. 2022). On the other hand, other studies have pointed out that the increase of dust temperature only arises from the sample selection bias, and no cosmological evolution in dust temperature at a given FIR luminosity is required (e.g., Dudzevičiūtė et al. 2020; Drew & Casey 2022). For the ALCS sample, this issue has already been discussed in Sun et al. (2022). They conclude that no evolution has been found in the

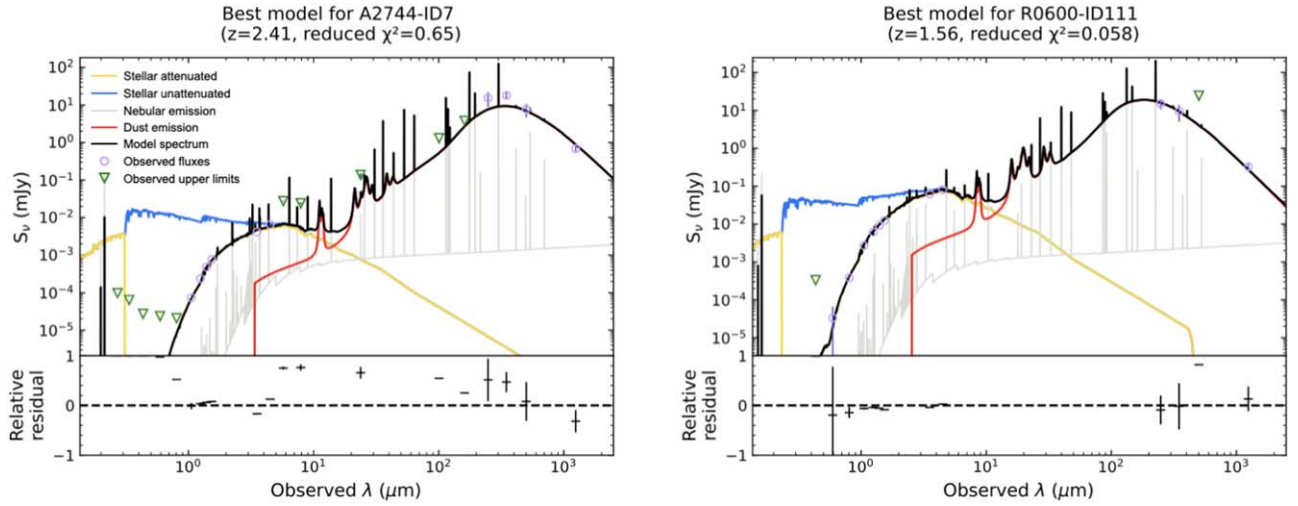


Figure 10. The SEDs of the galaxies that have especially high IRX. The SEDs are NOT corrected for lensing magnification. The colors and the symbols are the same as those in Figure 4.

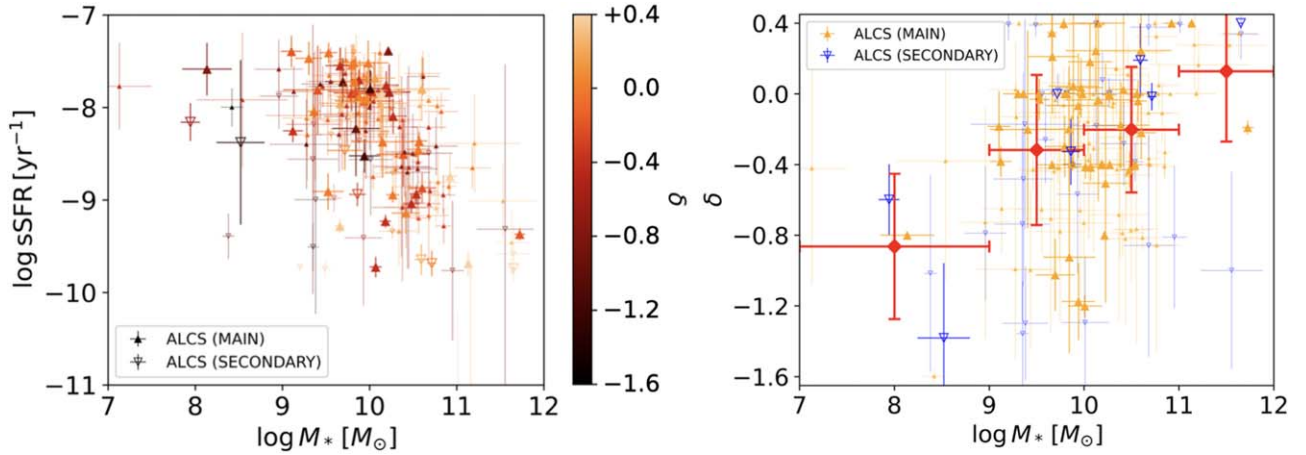


Figure 11. Left: the color-coded plot of δ (power-law index to modify the original Calzetti law, representing the steepness of the attenuation curve) on the sSFR vs. stellar mass plane. Right: Relation between δ and stellar mass. The red points show the mean values and standard deviations of δ in different stellar-mass bins. In these figures, the ALCS tier-1/2/3/4/5/6 samples are plotted. The large symbols show the galaxies that have spectroscopic redshifts, while the small symbols show those with photometric redshifts. The multiply imaged sources are plotted individually, but they are counted only once in deriving the average values. The stellar masses are corrected for lensing magnification.

dust temperatures of Luminous Infrared Galaxies (LIRGs) ($L_{\text{IR}} < 10^{12} L_{\odot}$) at $z \leq 2$ and ULIRGs ($L_{\text{IR}} > 10^{12} L_{\odot}$) at $z \simeq 1-4$. In this paper, we just discuss the robust properties of dust temperature in the ALCS sample and compare them with other SMG samples.

Figure 12 compares the dust temperatures obtained from major ALMA surveys. For a conservative discussion, we only plot the sources that are detected with Herschel over 2σ for the ALCS, ASPECS, and AS2UDS samples, where the dust temperatures are more reliably constrained than the other sources. For the same reason, the ALESS sample is limited to the well-sampled subset reported in da Cunha et al. (2021). One should be aware that these selections can cause biases, and the subsamples might not reflect the averaged properties of the whole samples. The left panel plots the characteristic dust temperature versus the dust luminosity. We confirm that the galaxies that have higher dust luminosities tend to have higher dust temperatures. This can be explained by the selection bias, that galaxies with colder dust are brighter in the sub/millimeter band in the same luminosity range. We also confirm that,

thanks to the lensing effect, the ALCS sample probes a broader range in lower dust luminosities than the conventional SMG samples (ALESS and AS2UDS) in the same temperature range. The right panel plots the characteristic dust temperature versus the redshift. The black solid and orange dashed lines show the average characteristic dust temperatures of the ALCS MAIN and the SECONDARY samples in each redshift bin, respectively. We confirm good agreement between the ALCS and the ASPECS samples, whereas a small systematic offset is found between the ALCS and the ALESS/AS2UDS samples. This discrepancy can also be attributed to the selection, showing that the ALCS sample includes sources with higher dust temperatures than the conventional SMG samples in the same redshift range.

We note that M0416-ID156 and A2537-ID24/66 (a multiply imaged source) exhibit especially high dust temperatures ($T_{\text{dust}} > 70$ K, corresponding to $T_{\text{dust}}^{\text{peak}} > 119$ K). These results might suggest an intense star formation activity in a compact morphology (Burnham et al. 2021) or a “dubbed starburst” as shown in Gómez-Guijarro et al. (2022b). However, we should

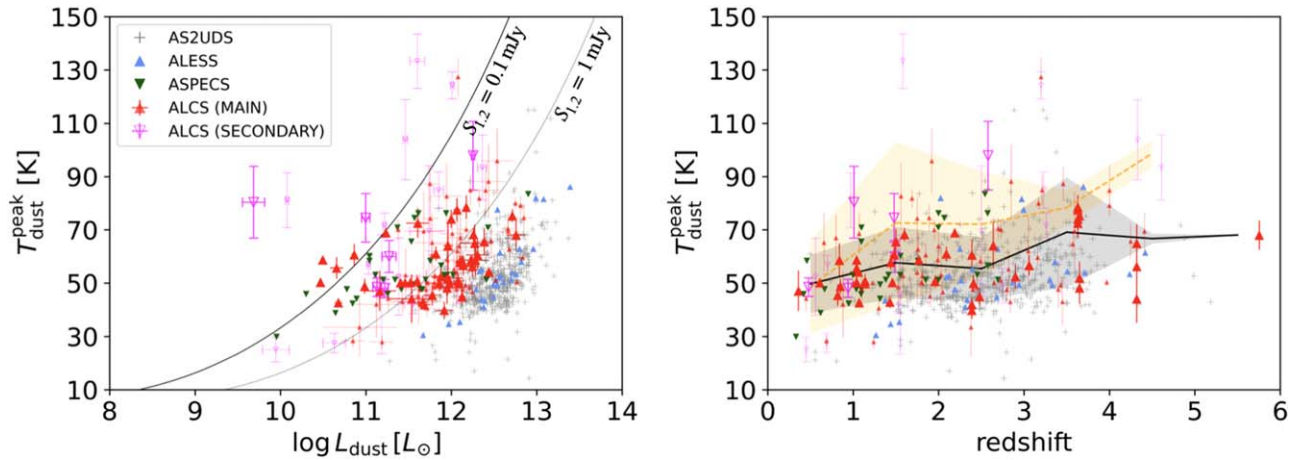


Figure 12. Left: Characteristic dust temperature vs. dust luminosity. The black solid and dotted lines represent the flux limit at 1.2 mm, where we assume an optically thin graybody with an emissivity index of 1.8 at $z = 3$. Right: Characteristic dust temperature vs. redshift. The black solid and orange dashed lines show the mean characteristic dust temperature of the MAIN and the SECONDARY samples in each redshift bin, respectively. The semitransparent regions show the standard deviations (i.e., $\pm 1\sigma$) from the mean values. In these plots, the ALCS, ASPECS, and AS2UDS samples are limited to the sources that are detected with Herschel over 2σ . The ALESS sample is also limited to the well-sampled subset reported in da Cunha et al. (2021). The large symbols show the galaxies that have spectroscopic redshifts, while the small symbols show those with photometric redshifts. The multiply imaged sources are plotted individually, but they are counted only once in deriving the average values. The dust luminosities are corrected for lensing magnification.

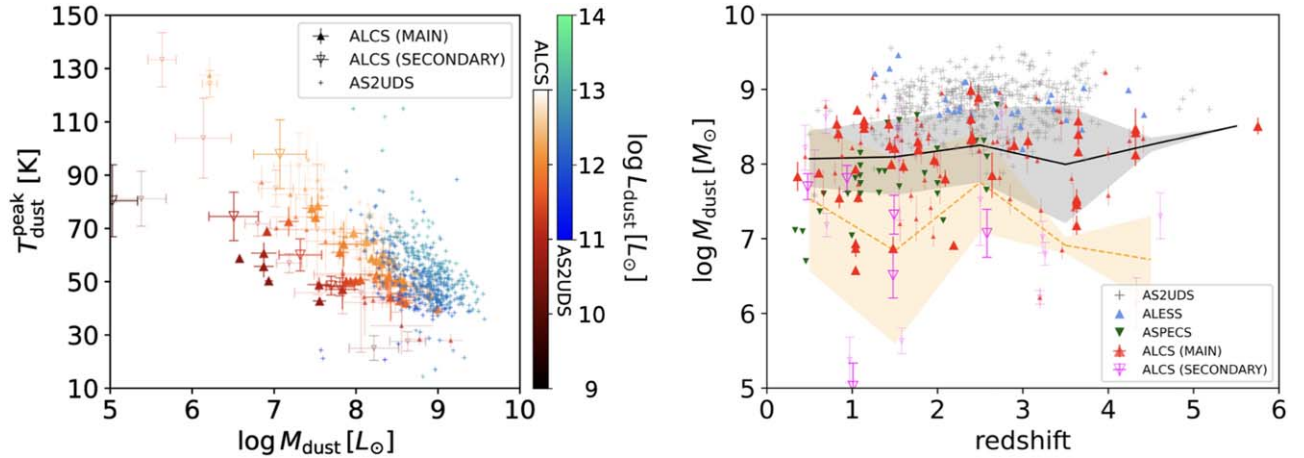


Figure 13. Left: Characteristic dust temperature vs. dust mass. The color bars show the dust luminosities. Right: Dust mass vs. redshift. The black solid and orange dashed lines show the mean dust mass for the MAIN and the SECONDARY samples in each redshift bin, respectively. The standard deviations are shown by the semitransparent regions. In these plots, the ALCS, ASPECS, and AS2UDS samples are limited to the sources that are detected with Herschel over 2σ . The ALESS sample is also limited to the well-sampled subset reported in da Cunha et al. (2021). The large symbols show the galaxies that have spectroscopic redshifts, while the small symbols show those with photometric redshifts. The multiply imaged sources are plotted individually. The dust masses and dust luminosities are corrected for lensing magnification.

be cautious about the potential uncertainty of the SED fitting. For instance, the FIR SED of M0416-ID156 is not well-fitted by the EThemis model. This may be attributed to the oversimplification of the model, and can cause large uncertainty in dust temperature and dust luminosity. Conversely, the SEDs of A2537-ID24/66 are fairly well-fitted. Nevertheless, there remains a possibility that their high dust temperatures are actually caused by the remaining blending effect of low-redshift sources. Future multiband observation with ALMA will be helpful to confirm the nature of these sources.

5.1.3. Dust Mass

The dust mass of a galaxy is also an essential parameter because dust is an efficient catalyst of molecular hydrogen formation in the interstellar medium (e.g., Gould & Salpeter 1963; Cazaux & Tielens 2004; Cazaux & Spaans 2009) and plays as a possible enhancer of star formation activities in the high-redshift

universe (Hirashita & Ferrara 2002). Since the dust mass of a galaxy is dominated by cold interstellar dust, submillimeter observations are suited for establishing a dust-mass-selected sample. Recently, Dudzevičiūtė et al. (2020) have suggested that the dust mass of AS2UDS sample is tightly correlated with the flux density at $870 \mu\text{m}$. Moreover, Dudzevičiūtė et al. (2021) have shown that $870 \mu\text{m}$ selection (AS2UDS) provides a more uniformly selected dust mass sample across $z = 1-6$ than $450 \mu\text{m}$ selection (STUDIES; Wang et al. 2017). Since the ALCS sample is selected by longer wavelengths than those of AS2UDS, it is expected to provide a uniformly selected dust mass sample like AS2UDS. However, the estimation of dust mass is sensitive to dust temperature and dust opacity da Cunha et al. (2021). Deep multiwavelength observations in FIR bands are needed to solve these degeneracies.

The left panel of Figure 13 compares the dust temperature, dust mass, and dust luminosity in the ALCS and the AS2UDS

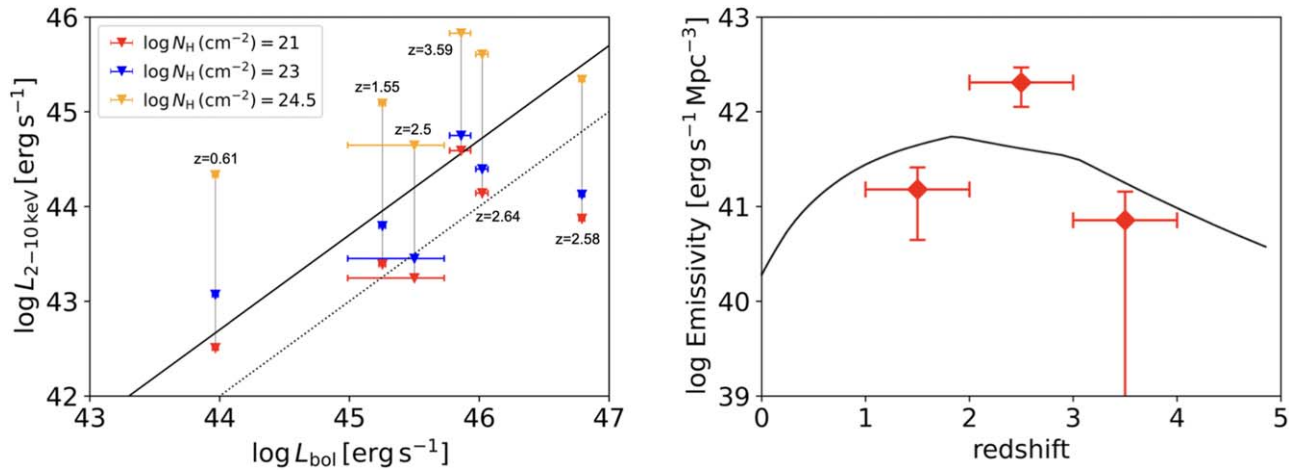


Figure 14. Left: X-ray luminosity upperbound with various assumptions of line-of-sight obscuration, plotted against bolometric AGN luminosity derived by SED analysis. The colors correspond to the line-of-sight hydrogen column density assumed in calculating the X-ray luminosity upperbound. The black solid line shows the empirical bolometric-to-X-ray luminosity relation of local AGNs ($L_{\text{bol}}/L_{2-10 \text{ keV}} = 20$; Vasudevan & Fabian 2007), and the black dotted line shows the “X-ray weak” case ($L_{\text{bol}}/L_{2-10 \text{ keV}} = 100$). In this plot, the AGN luminosities and X-ray luminosity upperbounds are corrected for lensing magnification. Right: Cosmological evolution of AGN luminosity density. The error bars only show the statistical errors that arise from the number of sources in each redshift bin. The black solid line shows that determined from X-ray surveys by Ueda et al. (2014).

samples. For a conservative discussion, we again impose the same FIR selections as those in Figure 12. We confirm that the ALCS sample contains galaxies with lower dust masses than the AS2UDS sample in the same dust temperature range. This can be attributed to the selection effect, showing that the ALCS sample is able to probe galaxies that have lower dust mass than the conventional SMG samples. The right panel plots dust mass versus redshift. The black solid and orange dashed lines show the average dust mass of the ALCS MAIN and the SECONDARY samples in each redshift bin, respectively. This figure shows that there is no obvious evolution in the mean dust mass of the ALCS sample, but the ALCS sample spreads widely in a lower dust mass range than the conventional SMG samples. Actually, as shown in the middle panel of Figure 6, ALCS MAIN sample behaves as a dust-mass-selected sample ranging $\log M_*/M_\odot = 8-9$ across $z = 1-6$ before the lensing correction. Therefore, the large scatter found in the dust mass of the ALCS sample just arises from the variation in the magnification factors.

5.2. AGN

In this subsection, we discuss the properties of the ALCS-nonXAGNs. We also discuss the cosmological evolution of the AGN luminosity density inferred from our sample.

5.2.1. Comparison with X-Ray Luminosity Upperbounds

The left panel of Figure 14 plots the X-ray luminosity upperbounds with various assumptions on line-of-sight obscuration, against the bolometric AGN luminosity derived by CIGALE. For comparison, we plot the empirical bolometric-to-X-ray luminosity relation of local AGNs ($L_{\text{bol}}/L_{2-10 \text{ keV}} = 20$; Vasudevan & Fabian 2007).³⁹ We find that most of the ALCS-nonXAGNs are consistent with their X-ray upperbands only in the heavily obscured cases, where the line-of-sight hydrogen column density ($N_{\text{H}}^{\text{LOS}}$) is over $10^{24.5} \text{ cm}^{-2}$. This suggests that

these AGNs are heavily obscured or Compton-thick AGNs. Recently, Simpson et al. (2017) have reported that the gas column density inferred from the dust surface density in the AS2UDS sample is $N_{\text{H}} = 9.8_{-0.7}^{+1.4} \times 10^{23} \text{ cm}^{-2}$, which is equivalent to the heavy-obscuration case in Figure 14. Hence, the heavy obscuration of our AGN sample might be attributed to the host galaxies. Moreover, it has been suggested that some AGNs in local ULIRGs show “X-ray weak” features ($\kappa_{2-10 \text{ keV}} > 100$; Teng et al. 2015; Yamada et al. 2021). If this is applicable in our sample, the ALCS-nonXAGNs can be consistent with their X-ray luminosity upperbounds even in the less obscured cases ($N_{\text{H}}^{\text{LOS}} \leq 10^{23} \text{ cm}^{-2}$).

5.2.2. Cosmological Evolution of AGN Luminosity Density

We calculate the cosmological evolution of the AGN luminosity density (growth rate of SMBHs) in high-redshift U/LIRGs ($10^{11} L_\odot < L_{\text{IR}} < 10^{13} L_\odot$). First, we estimate the average $L_{\text{AGN-to-IR}}$ ratio in redshift bins of $z = 1-2$, $z = 2-3$, and $z = 3-4$. These values are calculated by comparing the summed best-fit AGN luminosities and infrared luminosities of the U/LIRGs in the tier-1 sample in each redshift bin.⁴⁰ Then, we apply the luminosity ratio to the infrared luminosity density of high-redshift U/LIRGs and obtain the AGN luminosity density. The infrared luminosity density is calculated by integrating the infrared luminosity function derived by Fujimoto et al. (2023) over $10^{11} L_\odot < L_{\text{IR}} < 10^{13} L_\odot$. We note that the infrared luminosity mentioned in this subsection refers to the one that does not contain the AGN component (same as the dust luminosity from star formation activity).

The right panel of Figure 14 shows the cosmological evolution of AGN luminosity density inferred from the ALCS tier-1 sample (including ALCS-XAGNs). We also plot the AGN luminosity density estimated by X-ray surveys below 10 keV (Ueda et al. 2014). We confirm a possible excess at $z = 2-3$. This might show that a significant fraction of AGNs in this epoch are heavily obscured and might be missed in previous X-ray surveys. However, we must bear in mind that the AGN

³⁹ Note that this relationship has a large scatter ($L_{\text{bol}}/L_{2-10 \text{ keV}} = 6-400$) and shows potential strong dependence on the Eddington ratio (see also Lusso et al. 2012; Brightman et al. 2017 for other calibrations).

⁴⁰ For the ALCS-XAGNs, we employ the values derived by the SED analysis performed by Uematsu et al. (2023).

detection by SED analysis should have large uncertainties, and the results should highly depend on the model assumptions. Future sensitive hard X-ray (>10 keV) observations will be useful to reveal the nature of heavily obscured or Compton-thick AGNs in the high-redshift universe.

6. Summary

We report the multiwavelength properties of millimeter galaxies detected in the ALMA Lensing Cluster Survey (ALCS). The main conclusions are summarized as follows:

1. We performed UV to millimeter SED modeling of the whole ALCS sample (except for the cluster members and the ALCS-XAGNs), utilizing the photometric data obtained with HST, Spitzer, Herschel, and ALMA.
2. We confirm that the majority of the ALCS sources lie on the star-forming main sequence, while a smaller fraction shows intense starburst activities. This trend is the same as for other ALMA-detected SMG samples, e.g., ALESS, AS2UDS, and ASAGAO, although the ALCS sample contains galaxies with even lower SFRs and stellar masses thanks to the lensing effect.
3. We find two extremely dust-obscured galaxies (A2744-ID7 [$z=2.41$] and R0600-ID111 [$z=1.56$]). These galaxies have steeper attenuation slopes than the average, which may result in more UV absorption and hence higher IRX.
4. We confirm that the ALCS sample exhibits a wider range in dust temperatures than those in the conventional SMG samples (ALESS, and AS2UDS) in the same redshift range. We also confirm that the ALCS sample shows a large scatter in a lower dust mass range than those in the conventional SMG samples after lensing correction.
5. We identify six AGN candidates that are not detected in the archival Chandra data. The X-ray upperbounds indicate that these AGNs are heavily obscured or Compton-thick AGNs. We also find that the AGN luminosity density inferred from the ALCS tier-1 sample (including ALCS-XAGNs) shows a possible excess at $z=2-3$ compared with that determined from X-ray surveys below 10 keV (Ueda et al. 2014). This suggests that a significant fraction of AGNs in this epoch are

S.Y. is grateful for support from RIKEN Special Postdoctoral Researcher Program. We additionally acknowledge support from ANID—Millennium Science Initiative Program—ICN12_009 (FEB), CATA-BASAL—ACE210002 (FEB) and FB210003 (FEB), and FONDECYT Regular—1200495 (FEB). Numerical computations were carried out using the SuMIRE cluster operated by the Extragalactic OIR group at ASIAA. D.E. acknowledges support from a Beatriz Galindo senior fellowship (BG20/00224) from the Spanish Ministry of Science and Innovation, projects PID2020-114414GB-I00 and PID2020-113689GB-I00 financed by MCIN/AEI/10.13039/501100011033, project P20_00334 financed by the Junta de Andalucía, project A-FQM-510-UGR20 of the FEDER/Junta de Andalucía-Consejería de Transformación Económica, Industria, Conocimiento y Universidades.

Facilities: ALMA, CXO, HST, Spitzer, Herschel.

Software: CIGALE v2022.0 (Boquien et al. 2019; Yang et al. 2022), MAGPHYS high- z extension (v2) (da Cunha et al. 2015; Battisti et al. 2020), MAGPHYS photo- z extension (Battisti et al. 2019), HEAsoft v6.27 (Nasa High Energy Astrophysics Science Archive Research Center (Heasarc) 2014), CIAO v4.12 (Fruscione et al. 2006), CASA v5.4.0 (McMullin et al. 2007), SExtractor v2.5.0 (Bertin & Arnouts 1996), DustEM v4.2 (Compiègne et al. 2011).

Appendix A

Detailed Description of X-Ray Analysis and X-Ray Luminosity Upperbounds

The X-ray spectrum of an AGN mainly consists of three components: (1) a direct component from the nucleus, (2) reflection components from the torus and/or the accretion disk, and (3) a scattered component and emission from photoionized plasma. Since the emission from photoionized plasma is not dominant above rest-frame 2 keV, we exclude this component from our model. We disregard the reflection component from the accretion disk, whose interpretation is under debate (see, e.g., Ogawa et al. 2019). Furthermore, we do not consider the X-ray emission from star formation activity, which is much fainter than the AGN component above rest-frame 2 keV. Hence, in this study, we only consider a direct component, a reflection component from a torus, and a scattered component. This model is described as follows in the XSPEC terminology:

$$\text{model 1} = \text{phabs} * (\text{zphabs} * \text{cabs} * \text{zcutoffpl} + \text{const} * \text{zcutoffpl} + \text{atable}\{\text{xclumpy_v01_RC.fits}\} + \text{atable}\{\text{xclumpy_v01_RL.fits}\}). \quad (\text{A1})$$

heavily obscured by gas and dust and might be missed in the previous X-ray observations.

Acknowledgments

This publication uses data from the ALMA programs: ADS/JAO, ALMA #2018.1.00035.L, #2013.1.00999.S, and #2015.1.01425.S. This work has been financially supported by JSPS KAKENHI grant Nos. 22J22795 (R.U.), 20H01946 (Y.U.), 17H06130 (K.K., Y.U.), 19K14759 (Y.T.), 22K20391, 23K13154 (S.Y.), and 22H01266 (Y.T.). This work has also been supported by the NAOJ ALMA Scientific Research grant No. 2017-06B (K.K.). I.S. acknowledges support from STFC (ST/X001075/1).

1. The first term (phabs) represents the photoelectric absorption by our Galaxy, which is fixed at the value estimated from the source position using the method of Willingale et al. (2013).
2. The first term in the parentheses represents the direct component. The zphabs and cabs represent photoelectric absorption and Compton scattering by torus matter. The line-of-sight hydrogen column density is tested at $\log N_{\text{H}}^{\text{LOS}} = 21, 23, 24.5$. The photon index and cutoff energy are fixed at $\Gamma = 1.9$ and $E_{\text{cut}} = 370$ keV, respectively, as typical values of local AGNs (Ricci et al. 2017).
3. The second term in the parentheses represents the unabsorbed scattered component. The parameters of

`zcutoffpl` are linked to those of the direct component. We fix the scattered fraction (`const`) to 0.01 as a typical value (Ricci et al. 2017; Gupta et al. 2021).

- The third and fourth terms in the parentheses represent the reflection continuum and fluorescence lines from the torus. We model these components with the XCLUMPY model (Tanimoto et al. 2019). The photon index, cutoff energy, and normalization are linked to those of the direct component. We fixed the torus angular width at $\sigma = 20^\circ$. The inclination angle is fixed at $i = 30^\circ$ when $\log N_{\text{H}}^{\text{LOS}}/\text{cm}^{-2} = 21$, and $i = 70^\circ$ when $\log N_{\text{H}}^{\text{LOS}}/\text{cm}^{-2} = 23$ and 24.5. The equatorial hydrogen column density ($N_{\text{H}}^{\text{Equ}}$) is set to be consistent with the line-of-sight hydrogen column density and the torus geometry (see Equation (3) in Tanimoto et al. 2019).

X-ray spectra of distant AGNs are often analyzed with simpler models, such as an absorbed power-law model. Accordingly, we also estimate the X-ray luminosity upperbounds with a

simple model described as follows in the XSPEC terminology:

$$\text{model 2} = \text{phabs} * \text{zphabs} * \text{cabs} * \text{zcutoffpl}. \quad (\text{A2})$$

The meanings of each symbol in model 2 are the same as those in the direct component of model 1. The line-of-sight hydrogen column density, photon index, and cutoff energy are fixed to $\log N_{\text{H}}^{\text{LOS}}/\text{cm}^{-2} = 22$, $\Gamma = 1.9$, and $E_{\text{cut}} = 370$ keV, respectively.

Appendix B Detailed Description of SED Modeling

First, the ALCS tier-1/2/5/6 samples were analyzed with a basic parameter set, which is summarized in Table 2. This adequately reproduces all the SEDs ($\chi^2/\text{dof} < 5$) except for A2744-ID227. The left panel of Figure 15 shows the SED and the best-fit models of A2744-ID227 analyzed with the basic parameter set. We noticed a significant excess in the mid-infrared band, suggesting the existence of a type-2 AGN.

Table 2
Basic Parameter Set Used for the SED Modeling

Parameter	Symbol	Value	Reference
SFH (sfhdelayed)			
e-folding time of the main stellar population	τ_{main} [Myr]	100, 316, 1000, 3162, 10,000	
Age of the main stellar population	<code>age_{main}</code> [Myr]	100, 158, 251, 398, 631, 1000, 1585, 2512, 3981, 6310	
e-folding time of the late burst population	τ_{burst} [Myr]	100	
Age of the late burst population	<code>age_{burst}</code> [Myr]	5, 10, 50, 100	
Mass fraction of the late burst population	f_{burst}	0, 0.05, 0.1, 0.3	
SSP (bc03)			Bruzual & Charlot (2003)
IMF of the stellar model			Chabrier (2003)
Metallicity of the stellar model		0.02	
Dust Attenuation (dustatt_modified_starburst)			Calzetti et al. (2000)
The color excess of the nebular lines	$E(B - V)_{\text{lines}}$	0.1, 0.2, 0.4, 0.6, 0.8, 1.0, 1.2, 1.4, 1.6, 1.8, 2.0, 2.2, 2.4	
Reduction factor to apply $E(B - V)_{\text{lines}}$ to calculate the stellar continuum attenuation	$E(B - V)_{\text{factor}}$	0.44	
UV bump amplitude		0, 3 (MW)	
Power-law index to modify the attenuation curve	δ	-1.6, -1.2, -0.8, -0.4, 0.0, 0.4	
Dust Emission (EThemis)			
Mass fraction of the small hydrocarbon solids	q_{hac}	0.01, 0.02, 0.06	
Minimum radiation field	$\log U_{\text{min}}$	-1.0, -0.2, 0.4, 0.8, 1.2, 1.6, 2.0, 2.2, 2.4, 2.6, 2.8, 3.0, 3.2, 3.4, 3.6, 3.8	
Power-law index of the starlight intensity distribution	α	2.5	
Mass fraction of dust illuminated with $U = U_{\text{min}}$	$1 - \gamma$	0.95, 0.99	
AGN Emission (skirtor2016)			Stalevski et al. (2012, 2016)
Average edge-on optical depth at 9.7 μm	$\tau_{9.7}$	11	
Radial gradient of dust density	p	1.0	
Dust density gradient with polar angle	q	1.0	
Half-opening angle of the dust-free cone	Δ [$^\circ$]	40	
Ratio of outer to inner radius	R	20	
Inclination	θ [$^\circ$]	30, 70	
Fraction of AGN IR luminosity to total IR luminosity	f_{AGN}	0.0, 0.1, 0.3, 0.5, 0.7, 0.9 (0.0 for the SECONDARY sample)	
Extinction in polar direction	$E(B - V)$	0.3	
Temperature of the polar dust	T_{pol} [K]	150	

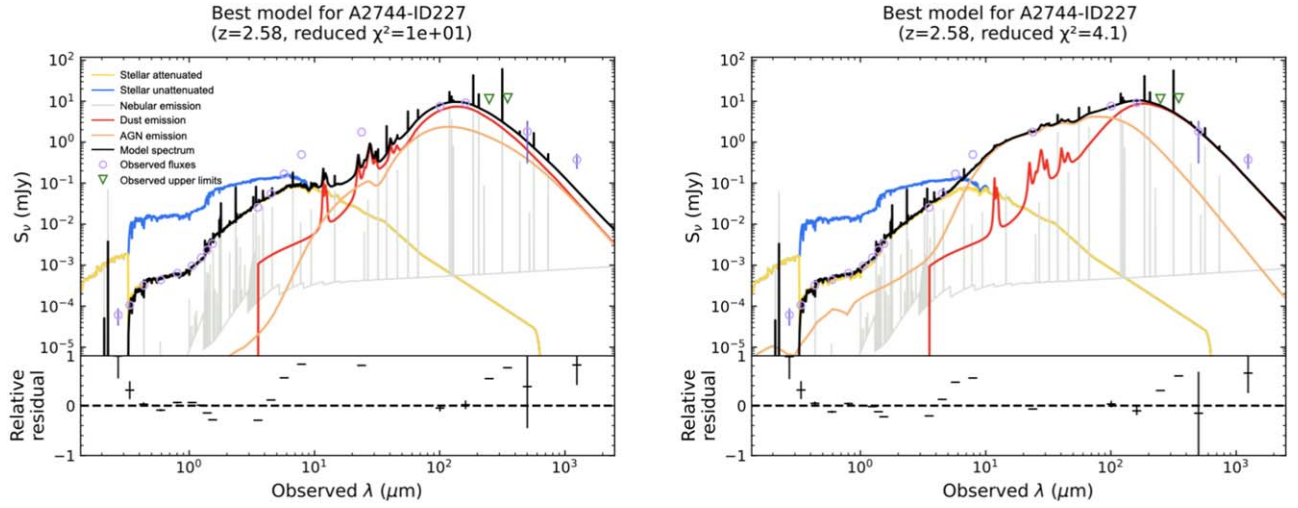


Figure 15. The SED and the best-fit model of A2744-ID227 analyzed with the basic parameter set (left panel) and those with the extended parameter set (right panel). The SEDs are NOT corrected for lensing magnification. The colors and the symbols are the same as those in Figure 4.

Table 3
Parameter Set of AGN Component Used for A2744-ID227

Parameter	Symbol	Value	Reference
AGN Emission (skirtor2016)			Stalevski et al. (2012, 2016)
Average edge-on optical depth at $9.7 \mu\text{m}$	$\tau_{9.7}$	3, 11	
Radial gradient of dust density	p	1.0	
Dust density gradient with polar angle	q	1.0	
Half-opening angle of the dust-free cone	$\Delta [^\circ]$	40	
Ratio of outer to inner radius	R	20	
Inclination	$\theta [^\circ]$	70	
Fraction of AGN IR luminosity to total IR luminosity	f_{AGN}	0.0, 0.1, 0.3, 0.5, 0.7, 0.9	
Extinction in polar direction	$E(B - V)$	0.0, 0.3	
Temperature of the polar dust	$T_{\text{pol}} [\text{K}]$	150	

Table 4
Parameter Set of Dust Emission Component Used for tier-3/4 Samples

Parameter	Symbol	Value
Dust Emission (EThemis)		
Mass fraction of the small hydrocarbon solids	q_{hac}	0.01
Minimum radiation field	$\log U_{\text{min}}$	-1.0, -0.2, 0.4, 0.8, 1.2, 1.6, 2.0, 2.2, 2.4, 2.6, 2.8, 3.0, 3.2, 3.4, 3.6, 3.8
Power-law index of the starlight intensity distribution	α	2.5
Mass fraction of dust illuminated with $U = U_{\text{min}}$	$1 - \gamma$	0.99

Hence, we reanalyzed the SED with an extended parameter set of the AGN module, which is given in Table 3. The right panel of Figure 15 shows the SED and the best-fit models of A2744-ID227 analyzed with the extended parameter set. This operation greatly improved the goodness of the fit for this object ($\chi^2/\text{dof} = 10.6 \rightarrow 4.1$). Second, the ALCS tier-3/4 sources were analyzed with a limited parameter set for the dust emission model to avoid unreasonable fitting results. This parameter set is summarized in Table 4. This adequately reproduces all the SEDs in the tier-3/4 samples ($\chi^2/\text{dof} < 5$).

The observed SEDs and best-fit models of all the objects are shown in Figure 16. We note that the best-fit SEDs of A383-ID50 and M0416-ID156 look inconsistent with the observed ALMA fluxes ($\log F_{\text{obs}[1.2 \text{ mm}]} / F_{\text{model}} > 1$). This may be caused by the oversimplification of the dust SED model. We also note that the best-fit SED of ACT0102-ID50 looks inconsistent with the photometric data of Herschel ($\log F_{\text{obs}[250 \mu\text{m}]} / F_{\text{model}} > 1$). This might be caused by the blending effect from nearby sources or additional star formation activities that are deeply embedded in dust and not detected in optical to near-infrared bands.

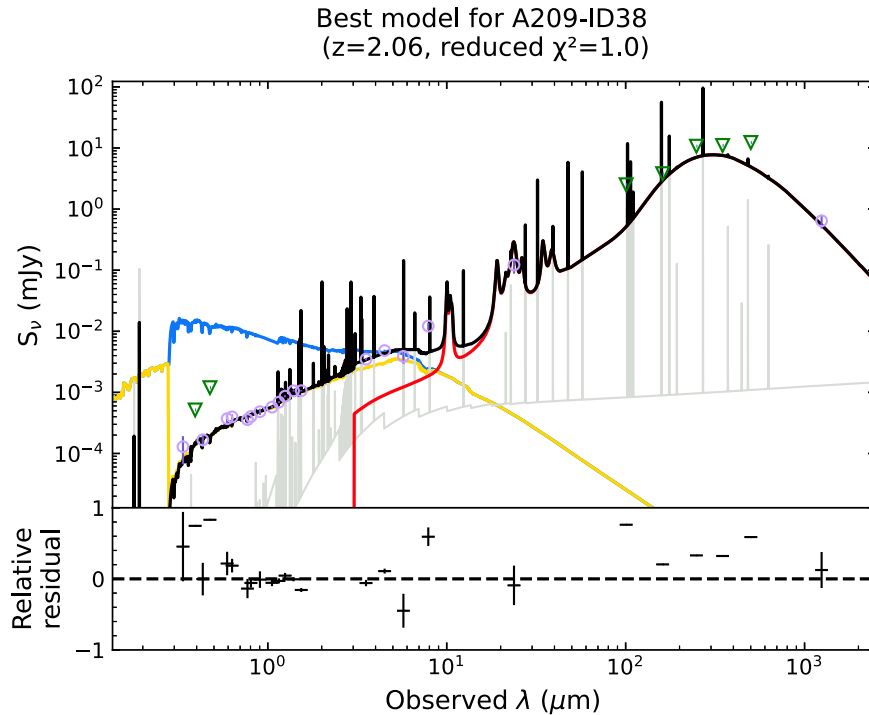


Figure 16. Example of the SED and the best-fit model of the ALCS sample. (The complete figure set of 160 images is available.)

Appendix C

Validity of Photometric Redshift and Impact of Redshift Uncertainty on Physical Properties

In this section, we discuss the validity of photometric redshifts and the impact of redshift uncertainty on physical properties. The photometric redshifts of the ALCS sources are estimated by several methods. For example, most of the photometric redshifts of tier-1/2/5/6 sources are estimated by an optical to near-infrared SED analysis with EAZY (Kokorev et al. 2022), whereas those of five objects (A2537-ID24, A2537-ID66, M0035-ID33, R0032-ID63, R0032-ID81) are taken from the literature, and those of two objects (ACT0102-ID223, ACT0102-ID294) are estimated by the sky positions and the lens model. The photometric redshifts of the tier-3/4/7/8 sources are estimated by near-infrared to millimeter SED analysis with a composite SED model obtained from AS2UDS sample (Dudzevičiūtė et al. 2020). To simplify the discussion, here, we only discuss the photometric redshifts estimated by EAZY.

First, we calculate the photometric redshifts of tier-1/2/5/6 sources by an optical to millimeter SED analysis with MAGPHYS photo- z extension (Battisti et al. 2019). Since the current version of MAGPHYS cannot treat an AGN component, the

ALCS-XAGNs and ALCS-nonXAGNs are not analyzed in this section. Figure 17 shows the results. The left panel plots photometric redshifts estimated by MAGPHYS photo- z extension versus spectroscopic ones. We confirm good agreement in those values, where 34/44 (77%) sources meet $|z_{\text{spec}} - z_{\text{photo}}|/(1 + z_{\text{spec}}) < 0.2$. The right panel plots photometric redshifts derived by MAGPHYS versus ones obtained by EAZY. We again confirm good agreement in those values, where 59/72 (82%) sources meet $|z_{\text{MAGPHYS}} - z_{\text{EAZY}}|/(1 + z_{\text{EAZY}}) < 0.2$.

Second, in order to evaluate the impact of redshift uncertainty on the derived physical properties, we independently estimate the physical parameters by an optical to millimeter SED analysis with MAGPHYS high- z extension (v2) (da Cunha et al. 2015; Battisti et al. 2020), where the redshifts are fixed at the photometric ones derived by EAZY. Figure 18 plots the physical properties estimated with variable redshifts versus those estimated at fixed redshifts. The standard deviations from the identity relations are 0.54 dex, 0.29 dex, 0.47 dex, 0.42 dex, and 6.1 K for SFR, stellar mass, dust luminosity, dust mass, and dust temperature, respectively. This indicates that the uncertainties in redshift measurement can cause at least these levels of uncertainties in each of the parameters.

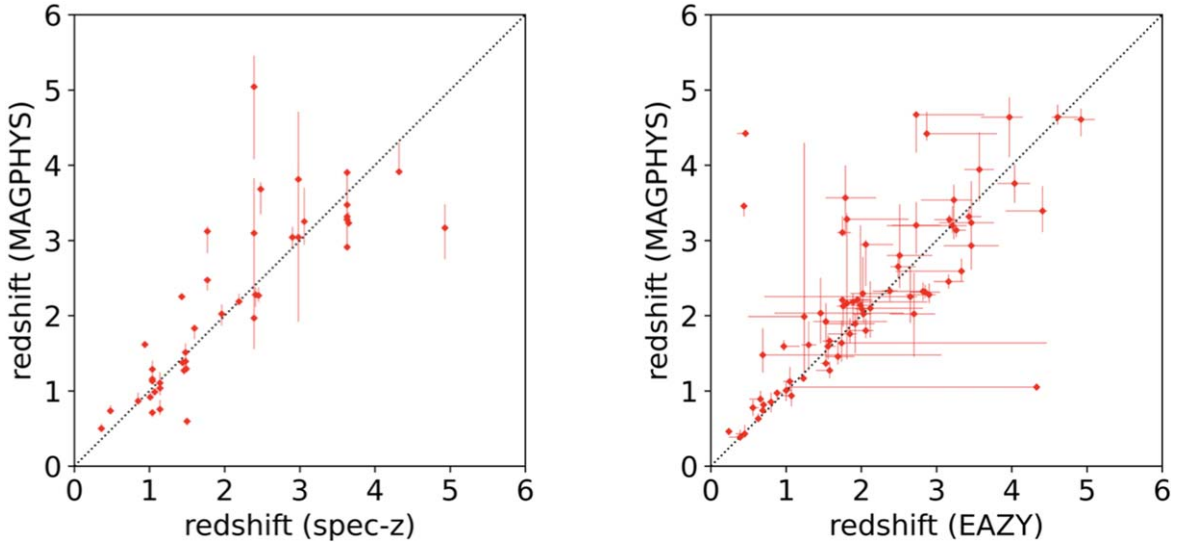


Figure 17. Left: comparison between spectroscopic redshift and photometric redshift estimated by MAGPHYS. Right: comparison between photometric redshift estimated by EAZY and that estimated by MAGPHYS. The black dotted lines show the identity relations.

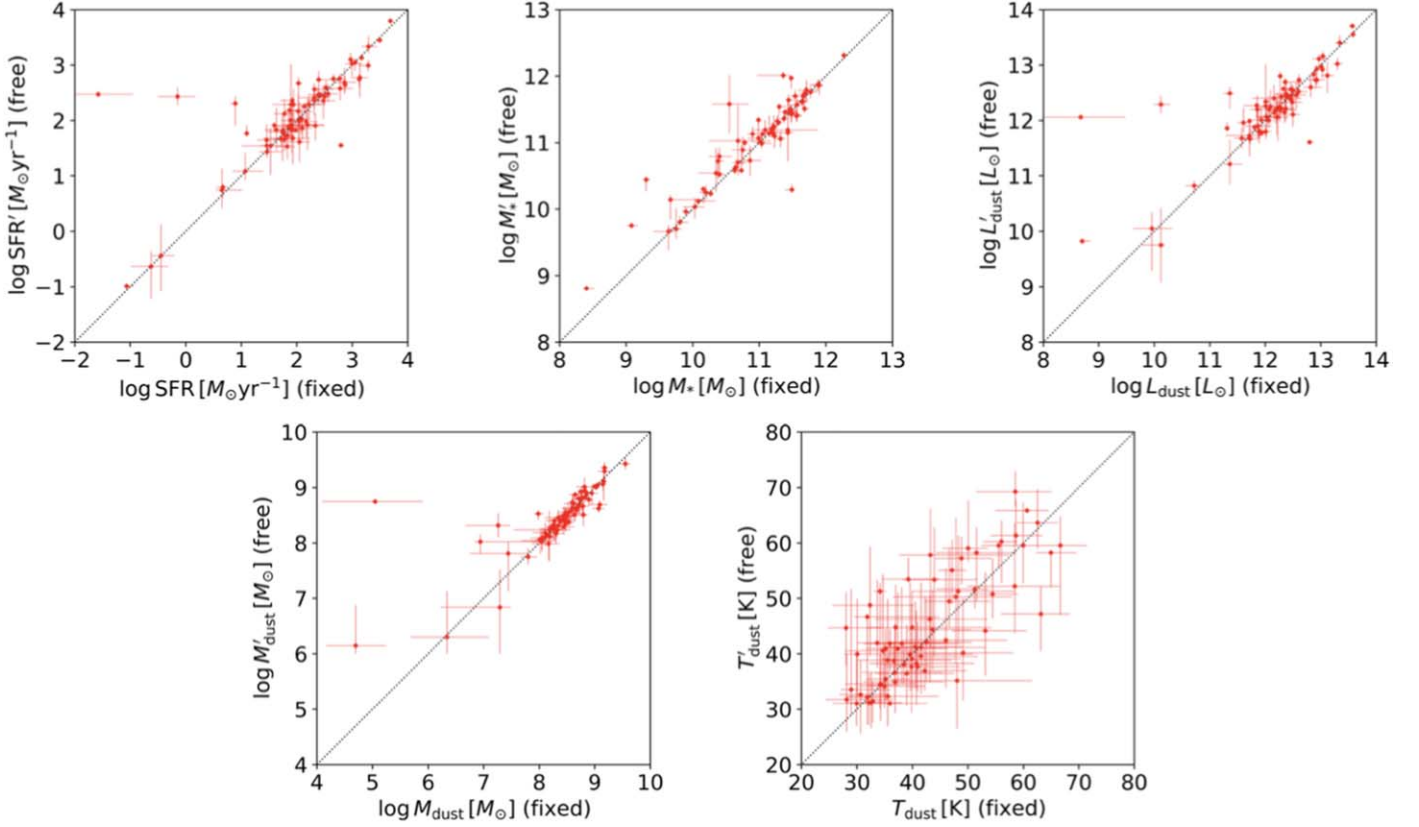


Figure 18. Comparison of the physical properties estimated with redshifts left as a free parameter (vertical axis) vs. those estimated at fixed redshifts (horizontal axis). The black dotted lines show the identity relations. The lensing magnification is not corrected for the SFR, stellar mass, dust luminosity, and dust mass.

Appendix D Comparison between CIGALE and MAGPHYS

In this section, we check possible systematic differences in the estimation of physical properties between CIGALE and MAGPHYS. See also Hunt et al. (2019), Pacifici et al. (2023) for comprehensive studies among some popular SED analysis codes. For a conservative discussion, we only discuss the tier-1 samples, where the physical properties are more reliably

constrained than the other samples. In addition, since the current version of MAGPHYS cannot treat an AGN component, ALCS-XAGNs and ALCS-nonXAGNs are excluded. Figure 19 compares the major physical properties estimated with CIGALE with those with MAGPHYS. We perform Passing-Bablok regression analysis for each parameter, where the conversion relation is shown at the bottom of each panel. We find good agreement for SFR, dust luminosity, and dust mass, while a large discrepancy is found for dust temperature

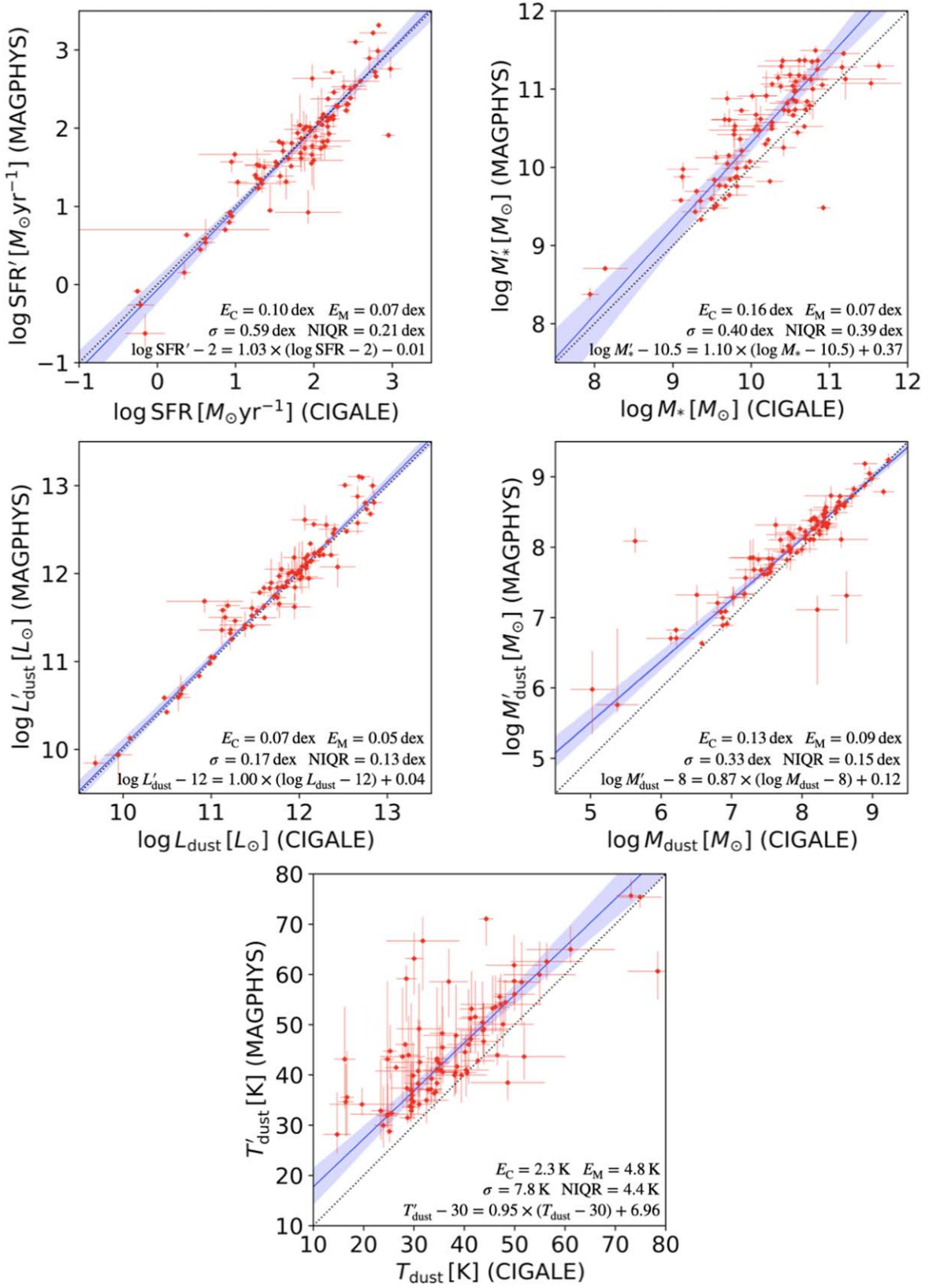


Figure 19. Comparison of SFR, stellar mass, dust luminosity, dust mass, and dust temperature measured by CIGALE and MAGPHYS. The blue solid lines show the regression lines, which are shown in the bottom equations in each panel. The semitransparent blue bands show the 95% confidence regions of each correlation. The standard deviations (σ) and normalized interquartile ranges (NIQR) around the regression lines measured in the vertical axes are shown at the bottom of each panel. We also show the median value of the statistical errors estimated with CIGALE (E_C) and MAGPHYS (E_M) for comparison. The black dotted lines show the identity relations. For a conservative discussion, only the tier-1 samples are plotted for the ALCS sample. The multiply imaged sources are plotted individually. The lensing magnification is corrected for the SFR, stellar mass, dust luminosity, and dust mass.

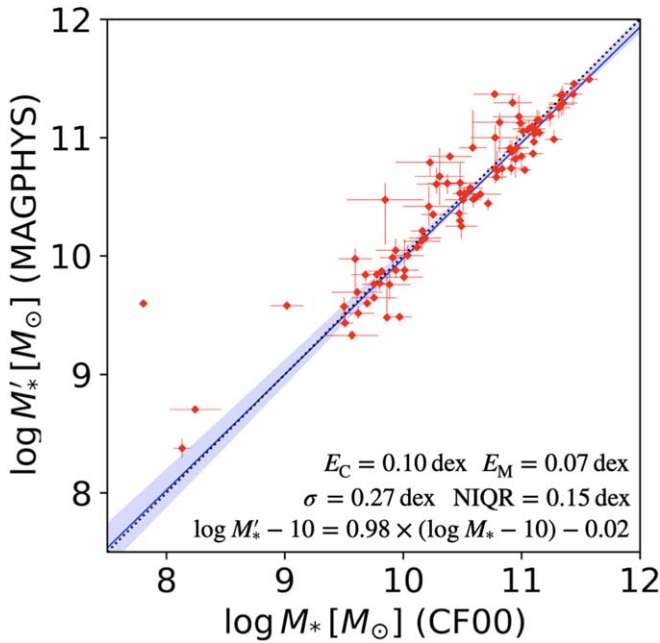


Figure 20. Comparison of stellar mass estimated with CIGALE using the Charlot & Fall (2000) model with that estimated with MAGPHYS. The symbols are the same as those in Figure 19. The lensing magnification is corrected for the stellar masses.

(~ 7 K at 30 K) and stellar mass (~ 0.37 dex at $\log M_*/M_\odot = 10.5$). These differences can be explained as follows:

1. The systematic difference in dust temperature can be attributed to its definition. In the EThemis model (used in CIGALE), dust temperature is defined as the intrinsic temperature of cold interstellar dust illuminated by a radiation field of $U = U_{\min}$. By contrast, in MAGPHYS, dust temperature is defined as the luminosity-weighted average of warm birth clouds and cold interstellar dust. Since dust temperature derived by MAGPHYS is also affected by the warm dust components, this value tends to be larger than that derived by CIGALE.
2. The systematic difference in stellar mass can be attributed to the difference in dust attenuation models. In this study, we use the modified Calzetti law in CIGALE, whereas the Charlot & Fall (2000) model is used in MAGPHYS. The modified Calzetti law assumes a single dust component (interstellar dust) with flexible attenuation curves. By contrast, the Charlot & Fall (2000) model assumes two dust components with fixed power-law attenuation slopes (interstellar dust and birth cloud). In the model of Charlot & Fall (2000), even near-infrared emission from young stars can be heavily attenuated by thick birth clouds. This may cause overestimation of intrinsic near-infrared luminosities, and hence stellar masses in MAGPHYS.⁴¹ In CIGALE, we can also choose the Charlot & Fall (2000) model for the dust attenuation model. In this case, we confirm good agreement between stellar mass estimated with CIGALE and that with MAGPHYS (Figure 20).

⁴¹ By contrast, stellar masses can be underestimated with CIGALE because of the simplified dust component, which may underestimate the near-infrared emission from young stars.

Moreover, we confirm that the standard deviations around the regression lines are 0.59 dex, 0.40 dex, 0.17 dex, 0.33 dex, and 7.8 K for SFR, stellar mass, dust luminosity, dust mass, and dust temperature, respectively. These values are significantly larger than the median statistical errors estimated with CIGALE and MAGPHYS. This indicates that the reported errors in the physical properties are fairly underestimated, considering the uncertainties in the SED models.

Appendix E Conversion Method of Dust Temperature

In this section, we summarize the conversion method of dust temperature among different definitions. First, for the ALESS sample, da Cunha et al. (2021) adopted a single optically thin graybody with various emissivity indices. In this case, characteristic dust temperature is calculated as follows:

$$T_{\text{dust}}^{\text{peak}} = [W(-(\beta + 3)e^{-\beta-3}) + \beta + 3]/2.821 \times T_{\text{dust}} \quad (\text{E1})$$

where W is the Lambert W function (principal branch), and β is the emissivity index. Second, for the AS2UDS sample, Dudzevičiūtė et al. (2020) estimated the dust temperatures by adopting a single optically thin graybody with an emissivity index of 1.8. This value is converted to the characteristic temperature by applying Equation (E1) assuming $\beta = 1.8$, which is described as follows:







$$T_{\text{dust}}^{\text{peak}} \simeq 1.7 \times T_{\text{dust}} \quad (\text{E2})$$

Third, in the case of the ALCS sample, as shown in Nersesian et al. (2019), the FIR emission from the EThemis model can be approximated by a graybody with an emissivity index of 1.79. Therefore, we convert the value by applying Equation (E2). Finally, for the ASPECS sample, Aravena et al. (2020) used MAGPHYS to estimate the dust temperature. Since MAGPHYS uses a complex dust emission model, it is difficult to obtain the conversion relation from the model itself. Hence, we utilize the conversion law between MAGPHYS and CIGALE denoted in Figure 19, and yield the conversion relation using Equation (E2), which is described as follows:

$$\begin{aligned} T_{\text{dust}}^{\text{peak}} &\simeq 1.7 * T_{\text{dust [CIGALE]}} \\ &\simeq 1.7 * (T_{\text{dust [MAGPHYS]}} - 8.3)/0.95. \end{aligned} \quad (\text{E3})$$

ORCID iDs

Ryosuke Uematsu <https://orcid.org/0000-0001-6653-779X>
 Yoshihiro Ueda <https://orcid.org/0000-0001-7821-6715>
 Kotaro Kohno <https://orcid.org/0000-0002-4052-2394>
 Yoshiki Toba <https://orcid.org/0000-0002-3531-7863>
 Satoshi Yamada <https://orcid.org/0000-0002-9754-3081>
 Ian Smail <https://orcid.org/0000-0003-3037-257X>
 Hideki Umehata <https://orcid.org/0000-0003-1937-0573>
 Seiji Fujimoto <https://orcid.org/0000-0001-7201-5066>
 Bunyo Hatsukade <https://orcid.org/0000-0001-6469-8725>
 Yiping Ao <https://orcid.org/0000-0003-3139-2724>
 Franz Erik Bauer <https://orcid.org/0000-0002-8686-8737>
 Gabriel Brammer <https://orcid.org/0000-0003-2680-005X>
 Miroslava Dessauges-Zavadsky <https://orcid.org/0000-0003-0348-2917>
 Daniel Espada <https://orcid.org/0000-0002-8726-7685>

Jean-Baptiste Jolly  <https://orcid.org/0000-0002-3405-5646>
 Anton M. Koekemoer  <https://orcid.org/0000-0002-6610-2048>
 Vasily Kokorev  <https://orcid.org/0000-0002-5588-9156>
 Georgios E. Magdis  <https://orcid.org/0000-0002-4872-2294>
 Masamune Oguri  <https://orcid.org/0000-0003-3484-399X>
 Fengwu Sun  <https://orcid.org/0000-0002-4622-6617>

References

- Algera, H. S. B., Smail, I., Dudzevičiūtė, U., et al. 2020, *ApJ*, 903, 138
 Álvarez-Márquez, J., Burgarella, D., Heinis, S., et al. 2016, *A&A*, 587, A122
 Aravena, M., Boogaard, L., González-López, J., et al. 2020, *ApJ*, 901, 79
 Aravena, M., Decarli, R., González-López, J., et al. 2019, *ApJ*, 882, 136
 Aravena, M., Decarli, R., Walter, F., et al. 2016a, *ApJ*, 833, 68
 Aravena, M., Decarli, R., Walter, F., et al. 2016b, *ApJ*, 833, 71
 Battisti, A. J., Cunha, E. d., Shivaie, I., & Calzetti, D. 2020, *ApJ*, 888, 108
 Battisti, A. J., da Cunha, E., Grasha, K., et al. 2019, *ApJ*, 882, 61
 Beckwith, S. V. W., Stiavelli, M., Koekemoer, A. M., et al. 2006, *AJ*, 132, 1729
 Bertin, E., & Arnouts, S. 1996, *A&AS*, 117, 393
 Blain, A. W., Smail, I., Ivison, R. J., Kneib, J. P., & Frayer, D. T. 2002, *PhR*, 369, 111
 Boogaard, L. A., Decarli, R., González-López, J., et al. 2019, *ApJ*, 882, 140
 Boogaard, L. A., van der Werf, P., Weiss, A., et al. 2020, *ApJ*, 902, 109
 Boquien, M., Buat, V., Burgarella, D., et al. 2022, *A&A*, 663, A50
 Boquien, M., Burgarella, D., Roehlly, Y., et al. 2019, *A&A*, 622, A103
 Bouchet, P., Lequeux, J., Maurice, E., Prevot, L., & Prevot-Burnichon, M. L. 1985, *A&A*, 149, 330
 Bouwens, R., González-López, J., Aravena, M., et al. 2020, *ApJ*, 902, 112
 Bouwens, R. J., Aravena, M., Decarli, R., et al. 2016, *ApJ*, 833, 72
 Brightman, M., Baloković, M., Ballantyne, D. R., et al. 2017, *ApJ*, 844, 10
 Bruzual, G., & Charlot, S. 2003, *MNRAS*, 344, 1000
 Burnham, A. D., Casey, C. M., Zavala, J. A., et al. 2021, *ApJ*, 910, 89
 Calzetti, D., Armus, L., Bohlin, R. C., et al. 2000, *ApJ*, 533, 682
 Calzetti, D., Kinney, A. L., & Storchi-Bergmann, T. 1994, *ApJ*, 429, 582
 Caputi, K. I., Caminha, G. B., Fujimoto, S., et al. 2021, *ApJ*, 908, 146
 Carilli, C. L., Chluba, J., Decarli, R., et al. 2016, *ApJ*, 833, 73
 Casey, C. M. 2012, *MNRAS*, 425, 3094
 Casey, C. M., Narayanan, D., & Cooray, A. 2014, *PhR*, 541, 45
 Cazaux, S., & Spaans, M. 2009, *A&A*, 496, 365
 Cazaux, S., & Tielens, A. G. G. M. 2004, *ApJ*, 604, 222
 Chabrier, G. 2003, *PASP*, 115, 763
 Charlot, S., & Fall, S. M. 2000, *ApJ*, 539, 718
 Chen, C.-C., Smail, I., Swinbank, A. M., et al. 2015, *ApJ*, 799, 194
 Ciesla, L., Gómez-Guijarro, C., Buat, V., et al. 2023, *A&A*, 672, A191
 Clements, D. L., Pearson, C., Farrah, D., et al. 2018, *MNRAS*, 475, 2097
 Coe, D., Salmon, B., Bradač, M., et al. 2019, *ApJ*, 884, 85
 Compiègne, M., Verstraete, L., Jones, A., et al. 2011, *A&A*, 525, A103
 Cooke, E. A., Smail, I., Swinbank, A. M., et al. 2018, *ApJ*, 861, 100
 Coppin, K., Halpern, M., Scott, D., et al. 2008, *MNRAS*, 384, 1597
 Cortese, L., Fritz, J., Bianchi, S., et al. 2014, *MNRAS*, 440, 942
 da Cunha, E., Charlot, S., & Elbaz, D. 2008, *MNRAS*, 388, 1595
 da Cunha, E., Hodge, J. A., Casey, C. M., et al. 2021, *ApJ*, 919, 30
 da Cunha, E., Walter, F., Smail, I. R., et al. 2015, *ApJ*, 806, 110
 Danielson, A. L. R., Swinbank, A. M., Smail, I., et al. 2017, *ApJ*, 840, 78
 Decarli, R., Aravena, M., Boogaard, L., et al. 2020, *ApJ*, 902, 110
 Decarli, R., Smail, I., Walter, F., et al. 2014, *ApJ*, 780, 115
 Decarli, R., Walter, F., Aravena, M., et al. 2016a, *ApJ*, 833, 69
 Decarli, R., Walter, F., Aravena, M., et al. 2016b, *ApJ*, 833, 70
 Decarli, R., Walter, F., González-López, J., et al. 2019, *ApJ*, 882, 138
 Drew, P. M., & Casey, C. M. 2022, *ApJ*, 930, 142
 Dudzevičiūtė, U., Smail, I., Swinbank, A. M., et al. 2020, *MNRAS*, 494, 3828
 Dudzevičiūtė, U., Smail, I., Swinbank, A. M., et al. 2021, *MNRAS*, 500, 942
 Dunlop, J. S., McLure, R. J., Biggs, A. D., et al. 2017, *MNRAS*, 466, 861
 Franco, M., Elbaz, D., Béthermin, M., et al. 2018, *A&A*, 620, A152
 Franco, M., Elbaz, D., Zhou, L., et al. 2020a, *A&A*, 643, A30
 Franco, M., Elbaz, D., Zhou, L., et al. 2020b, *A&A*, 643, A53
 Fruscione, A., McDowell, J. C., Allen, G. E., et al. 2006, *Proc. SPIE*, 6270, 62701V
 Fudamoto, Y., Oesch, P. A., Magnelli, B., et al. 2020, *MNRAS*, 491, 4724
 Fujimoto, S., Kohno, K., Ouchi, M., et al. 2023, arXiv:2303.01658
 Fujimoto, S., Oguri, M., Brammer, G., et al. 2021, *ApJ*, 911, 99
 Fujimoto, S., Ouchi, M., Kohno, K., et al. 2018, *ApJ*, 861, 7
 Geach, J. E., Dunlop, J. S., Halpern, M., et al. 2017, *MNRAS*, 465, 1789
 Gómez-Guijarro, C., Elbaz, D., Xiao, M., et al. 2022a, *A&A*, 658, A43
 Gómez-Guijarro, C., Elbaz, D., Xiao, M., et al. 2022b, *A&A*, 659, A196
 González-López, J., Bauer, F. E., Romero-Cañizales, C., et al. 2017, *A&A*, 597, A41
 González-López, J., Novak, M., Decarli, R., et al. 2020, *ApJ*, 897, 91
 Gould, R. J., & Salpeter, E. E. 1963, *ApJ*, 138, 393
 Gullberg, B., Smail, I., Swinbank, A. M., et al. 2019, *MNRAS*, 490, 4956
 Gupta, K. K., Ricci, C., Tortosa, A., et al. 2021, *MNRAS*, 504, 428
 Hatsukade, B., Kohno, K., Yamaguchi, Y., et al. 2018, *PASJ*, 70, 105
 Hirashita, H., & Ferrara, A. 2002, *MNRAS*, 337, 921
 Hodge, J. A., & da Cunha, E. 2020, *RSOS*, 7, 200556
 Hodge, J. A., Karim, A., Smail, I., et al. 2013, *ApJ*, 768, 91
 Hunt, L. K., De Looze, I., Boquien, M., et al. 2019, *A&A*, 621, A51
 Inami, H., Decarli, R., Walter, F., et al. 2020, *ApJ*, 902, 113
 Inoue, A. K. 2011, *MNRAS*, 415, 2920
 Jolly, J.-B., Knudsen, K., Laporte, N., et al. 2021, *A&A*, 652, A128
 Jones, A. P., Köhler, M., Ysard, N., Bocchio, M., & Verstraete, L. 2017, *A&A*, 602, A46
 Karim, A., Swinbank, A. M., Hodge, J. A., et al. 2013, *MNRAS*, 432, 2
 Kashyap, V. L., van Dyk, D. A., Connors, A., et al. 2010, *ApJ*, 719, 900
 Kohno, K., Fujimoto, S., Tsujita, A., et al. 2023, arXiv:2305.15126
 Kokorev, V., Brammer, G., Fujimoto, S., et al. 2022, *ApJS*, 263, 38
 Kokorev, V., Jin, S., Magdis, G. E., et al. 2023, *ApJL*, 945, L25
 Komatsu, E., Smith, K. M., Dunkley, J., et al. 2011, *ApJS*, 192, 18
 Koprowski, M. P., Coppin, K. E. K., Geach, J. E., et al. 2020, *MNRAS*, 492, 4927
 Kormendy, J., & Ho, L. C. 2013, *ARA&A*, 51, 511
 Laporte, N., Zitrin, A., Ellis, R. S., et al. 2021, *MNRAS*, 505, 4838
 Lequeux, J., Maurice, E., Prevot-Burnichon, M. L., Prevot, L., & Rocca-Volmerange, B. 1982, *A&A*, 113, L15
 Lotz, J. M., Koekemoer, A., Coe, D., et al. 2017, *ApJ*, 837, 97
 Lusso, E., Comastri, A., Simmons, B. D., et al. 2012, *MNRAS*, 425, 623
 Madau, P., & Dickinson, M. 2014, *ARA&A*, 52, 415
 Magnelli, B., Boogaard, L., Decarli, R., et al. 2020, *ApJ*, 892, 66
 Magorrian, J., Tremaine, S., Richstone, D., et al. 1998, *AJ*, 115, 2285
 Marconi, A., & Hunt, L. K. 2003, *ApJL*, 589, L21
 McMullin, J. P., Waters, B., Schiebel, D., Young, W., & Golap, K. 2007, in ASP Conf. Ser. 376, *Astronomical Data Analysis Software and Systems XVI*, ed. R. A. Shaw, F. Hill, & D. J. Bell (San Francisco, CA: ASP), 127
 Nandy, K., Morgan, D. H., Willis, A. J., et al. 1980, *Natur*, 283, 725
 Nandy, K., Thompson, G. I., Jamar, C., Monfils, A., & Wilson, R. 1975, *A&A*, 44, 195
 Narayanan, D., Davé, R., Johnson, B. D., et al. 2018, *MNRAS*, 474, 1718
 Nasa High Energy Astrophysics Science Archive Research Center (Heasarc) 2014, HEASoft: Unified Release of FTOOLS and XANADU, Astrophysics Source Code Library, ascl:1408.004
 Nersesian, A., Xilouris, E. M., Bianchi, S., et al. 2019, *A&A*, 624, A80
 Ogawa, S., Ueda, Y., Yamada, S., Tanimoto, A., & Kawaguchi, T. 2019, *ApJ*, 875, 115
 Oguri, M. 2010, *PASJ*, 62, I017
 Pacifici, C., Iyer, K. G., Mobasher, B., et al. 2023, *ApJ*, 944, 141
 Pei, Y. C. 1992, *ApJ*, 395, 130
 Pettini, M., Kellogg, M., Steidel, C. C., et al. 1998, *ApJ*, 508, 539
 Planck Collaboration, Abergel, A., Ade, P. A. R., et al. 2011, *A&A*, 536, A25
 Popping, G., Pillepich, A., Somerville, R. S., et al. 2019, *ApJ*, 882, 137
 Popping, G., Puglisi, A., & Norman, C. A. 2017, *MNRAS*, 472, 2315
 Popping, G., Walter, F., Behroozi, P., et al. 2020, *ApJ*, 891, 135
 Postman, M., Coe, D., Benítez, N., et al. 2012, *ApJS*, 199, 25
 Prevot, M. L., Lequeux, J., Maurice, E., Prevot, L., & Rocca-Volmerange, B. 1984, *A&A*, 132, 389
 Reddy, N. A., Erb, D. K., Pettini, M., Steidel, C. C., & Shapley, A. E. 2010, *ApJ*, 712, 1070
 Ricci, C., Trakhtenbrot, B., Koss, M. J., et al. 2017, *ApJS*, 233, 17
 Rocca-Volmerange, B., Prevot, L., Ferlet, R., Lequeux, J., & Prevot-Burnichon, M. L. 1981, *A&A*, 99, L5
 Salim, S., Boquien, M., & Lee, J. C. 2018, *ApJ*, 859, 11
 Schreiber, C., Elbaz, D., Pannella, M., et al. 2018, *A&A*, 609, A30
 Schreiber, C., Pannella, M., Elbaz, D., et al. 2015, *A&A*, 575, A74
 Schwarz, G. 1978, *AnSta*, 6, 461
 Simpson, J. M., Smail, I., Swinbank, A. M., et al. 2017, *ApJ*, 839, 58
 Simpson, J. M., Swinbank, A. M., Smail, I., et al. 2014, *ApJ*, 788, 125
 Smail, I., Dudzevičiūtė, U., Stach, S. M., et al. 2021, *MNRAS*, 502, 3426
 Smit, R., Bouwens, R. J., Labbé, I., et al. 2016, *ApJ*, 833, 254
 SSC And IRSA 2020, Spitzer Enhanced Imaging Products, IPAC, doi:10.26131/IRSA433

- Stach, S. M., Dudzevičiūtė, U., Smail, I., et al. 2019, *MNRAS*, 487, 4648
- Stach, S. M., Smail, I., Swinbank, A. M., et al. 2018, *ApJ*, 860, 161
- Stalevski, M., Fritz, J., Baes, M., Nakos, T., & Popovič, L. 2012, *MNRAS*, 420, 2756
- Stalevski, M., Ricci, C., Ueda, Y., et al. 2016, *MNRAS*, 458, 2288
- Steinhardt, C. L., Jauzac, M., Acebron, A., et al. 2020, *ApJS*, 247, 64
- Sun, F., Egami, E., Fujimoto, S., et al. 2022, *ApJ*, 932, 77
- Swinbank, A. M., Karim, A., Smail, I., et al. 2012a, *MNRAS*, 427, 1066
- Swinbank, A. M., Simpson, J. M., Smail, I., et al. 2014, *MNRAS*, 438, 1267
- Swinbank, M., Smail, I., Karim, A., et al. 2012b, *Msngr*, 149, 40
- Takeuchi, T. T., Yuan, F.-T., Ikeyama, A., Murata, K. L., & Inoue, A. K. 2012, *ApJ*, 755, 144
- Tanimoto, A., Ueda, Y., Odaka, H., et al. 2019, *ApJ*, 877, 95
- Teng, S. H., Rigby, J. R., Stern, D., et al. 2015, *ApJ*, 814, 56
- Thomson, A. P., Ivison, R. J., Simpson, J. M., et al. 2014, *MNRAS*, 442, 577
- Toba, Y., Goto, T., Oi, N., et al. 2020, *ApJ*, 899, 35
- Ueda, Y., Akiyama, M., Hasinger, G., Miyaji, T., & Watson, M. G. 2014, *ApJ*, 786, 104
- Ueda, Y., Akiyama, M., Ohta, K., & Miyaji, T. 2003, *ApJ*, 598, 886
- Ueda, Y., Hatsukade, B., Kohno, K., et al. 2018, *ApJ*, 853, 24
- Uematsu, R., Ueda, Y., Kohno, K., et al. 2023, *ApJ*, 945, 121
- Uzgil, B. D., Carilli, C., Lidz, A., et al. 2019, *ApJ*, 887, 37
- Uzgil, B. D., Oesch, P. A., Walter, F., et al. 2021, *ApJ*, 912, 67
- Vasudevan, R. V., & Fabian, A. C. 2007, *MNRAS*, 381, 1235
- Viero, M. P., Sun, G., Chung, D. T., Moncelsi, L., & Condon, S. S. 2022, *MNRAS*, 516, L30
- Walter, F., Decarli, R., Aravena, M., et al. 2016, *ApJ*, 833, 67
- Wang, S. X., Brandt, W. N., Luo, B., et al. 2013, *ApJ*, 778, 179
- Wang, W.-H., Lin, W.-C., Lim, C.-F., et al. 2017, *ApJ*, 850, 37
- Weiß, A., Kovács, A., Coppin, K., et al. 2009, *ApJ*, 707, 1201
- Whitaker, K. E., Franx, M., Leja, J., et al. 2014, *ApJ*, 795, 104
- Willingale, R., Starling, R. L. C., Beardmore, A. P., Tanvir, N. R., & O'Brien, P. T. 2013, *MNRAS*, 431, 394
- Yamada, S., Ueda, Y., Tanimoto, A., et al. 2021, *ApJS*, 257, 61
- Yamaguchi, Y., Kohno, K., Hatsukade, B., et al. 2019, *ApJ*, 878, 73
- Yamaguchi, Y., Kohno, K., Hatsukade, B., et al. 2020, *PASJ*, 72, 69
- Yang, G., Boquien, M., Brandt, W. N., et al. 2022, *ApJ*, 927, 192
- Zhou, L., Elbaz, D., Franco, M., et al. 2020, *A&A*, 642, A155